# Probabilistic Safety Assessment of Nuclear Power Plants considering Climate Change

*Thomas Matteo Coscia* [a], *Francesco Di Maio* [a*], *Gyunyoung Heo* [b], *Enrico Zio* [a, c]

[a] Energy Department, Politecnico di Milano, Via La Masa 34, Milano 20156, Italy

[b] Kyung Hee University, 1732, Deogyeong-daero, Giheung-gu, Yongin-si, Gyeonggi-do 17104, Republic of Korea

[c] Mines Paris, PSL Centre de Recherche sur le Risques et les Crises, Sophia Antipolis 06904, France

*** Corresponding author e-mail:** *francesco.dimaio@polimi.it*

**Abstract**

Probabilistic Safety Assessment (PSA) of Nuclear Power Plants (NPPs) must take into account the impact of Climate Change (CC). In this paper, to do this, a PSA framework is developed coupling a CC impact assessment model, a source term estimation model, an atmospheric dispersion model and a groundwater contaminant transport model. The impact of CC on aquifer contamination is analyzed in terms of *i*) increase of accident initiating event frequencies due to CC-induced natural events and *ii*) alteration of hydrological conditions due to the CC influence on physical variables (e.g., temperature and precipitation) that affect atmospheric dispersion and groundwater transport of radioactive contaminant. An application of the proposed framework is performed with regards to the estimation of the peak dose following a hypothetical severe accident in a NPP site in South Korea. Under the assumptions made, CC is found to worsen the consequences of such accident in terms of groundwater radioactive contamination.

**Keywords:** *Probabilistic Safety Assessment (PSA), Nuclear Power Plant (NPP), Climate Change (CC), Atmospheric Dispersion, Groundwater Contamination*

## Nomenclature

### *Acronyms*

| | |
|---|---|
| ADE | Advection Dispersion Equation |
| AIC | Akaike Information Criterion |
| CBC | Climatic Boundary Condition |
| CC | Climate Change |
| CCDF | Complementary Cumulative Distribution Function |
| CDF | Core Damage Frequency |
| CMIP6 | Coupled Model Intercomparison Project phase 6 |
| CVaR | Conditional Value at Risk |
| ETs | Event Trees |
| FTs | Fault Trees |
| GCMs | Global Circulation Models |
| HYSPLIT | HYbrid Single-Particle Lagrangian Integrated Trajectory |
| IEs | Initiating Events |
| LOCA | Loss Of Coolant Accident |
| NPPs | Nuclear Power Plants |
| PDF | Probability Density function |
| PDSs | Plant Damage States |
| PMF | Probability Mass Function |
| PSA | Probabilistic Safety Assessment |
| RF | Release Fraction |
| RPV | Reactor Pressure Vessel |
| SB | Station Blackout |
| SSCs | Structures, Systems and Components (SSCs) |
| SSP | Shared Socioeconomic Pathway |
| ST | Source Term |
| STC | Source Term Category |
| SGTR | Steam Generator Tube Rupture |

### *Symbols*

| | |
|---|---|
| $\varepsilon_i$ | Fragility factor of the *i*-th IE |
| $\alpha_i$ | Factor of change of the external *i*-th IE frequency |
| $\alpha_{SB}$ | Factor of change of the SB frequency |
| $\alpha_{SGTR}$ | Factor of change of the SGTR frequency |
| $\alpha_{LOCA}$ | Factor of change of the LOCA frequency |
| $\beta$ | Factor of change of the infiltration flux |
| $f_i$ | External *i*-th IE frequency |
| $\dot{\psi}$ | Aquifer infiltration flux |
| $\bar{m}$ | Database listing climatic data |
| $\bar{m}_a$ | Database listing meteorological data |
| $t$ | Time |
| $i$ | IE index |
| $I$ | Total number of IEs |
| $n$ | Number of NPP units simultaneously affected by the IE |
| $N$ | Total number of units |
| $\lambda$ | Parameter of the truncated discrete exponential PMF |
| $f^j$ | Frequency of the *j*-th STC |
| $j$ | STC index |
| $J$ | Total number of STCs |
| $\bar{R}^j$ | RF vector of the *j*-th STC |
| $t_0$ | Current time |
| $T$ | Projection reference time for $\bar{m}$ |
| $\rho$ | Pearson correlation coefficient |
| $\mathcal{F}_i(\cdot)$ | Fragility curve of the $i$-th IE |
| $\mathcal{T}_r(\cdot)$ | Return time |
| $\Lambda$ | Truncated Poisson distribution parameter |
| $p$ | Truncated Negative Binomial distribution parameter |
| $k$ | Truncated Negative Binomial distribution parameter |
| $\eta$ | Truncated Negative Binomial distribution parameter |
| $w$ | Truncated Negative Binomial distribution parameter |
| $N_m$ | Number of different meteorological data records |
| $C_r$ | Concentration of $r$-th radionuclide in the compliance well |
| $D$ | Dose from contaminated groundwater ingestion |
| $r$ | Radionuclide index |
| $R$ | Total number of radionuclide species |
| $\dot{P}$ | Precipitation flux |
| $\dot{E}T$ | Evapotranspiration flux |
| $\dot{I}r$ | Irrigation flux |
| $\dot{R}$ | Runoff flux |
| $D_{peak}$ | Peak yearly dose from groundwater ingestion |
| $t_{peak}$ | Breakthrough time |
| $DC_r$ | *r*-th radionuclide dose conversion factor |
| $V_w$ | Total volume of water consumed by an adult in one year |
| $N_s$ | Number of Monte Carlo simulation trials for the deposited ST estimation |
| $s$ | Monte Carlo trial index (ST estimation) |
| $N_g$ | Number of Monte Carlo simulation trials for the peak dose estimation |
| $g$ | Monte Carlo trial index (peak dose estimation) |
| $\mathcal{U}\{\cdot\}$ | Uniform PMF |
| $Q_{sat}$ | Aquifer volumetric flowrate |
| $K$ | Hydraulic conductivity |
| $\nabla h$ | Hydraulic gradient |
| $\mathbb{E}[\cdot]$ | Expectation operator |
| $N_{ex}$ | Number of simulations in which $D_{peak} > \tau$ |
| $\tau$ | Regulatory threshold |
| $CVaR(\cdot)$ | Conditional Value at Risk |
| $P_{ex}$ | Exceedance probability |
| $\Delta CVaR(\cdot)$ | Relative difference between CVaR values |
| $\Delta P_{ex}$ | Relative difference between $P_{ex}$ values |
| $A_{sat}$ | Aquifer cross section area (saturated zone) |
| $\alpha_L$ | Longitudinal dispersivity |
| $K_d$ | Distribution coefficient |
| $S_{l,sat}$ | Water saturation level (saturated zone) |
| $S_{l,unsat}$ | Water saturation level (unsaturated zone) |
| $x_{sat}$ | Length of the saturated zone |
| $x_{unsat}$ | Length of the unsaturated zone |
| $y_{sat}$ | Thickness of the saturated zone |
| $y_{unsat}$ | Thickness of the unsaturated zone |
| $z_{source}$ | Depth of the deposited source term |
| $z_{sat}$ | Depth of the saturated zone |
| $z_{unsat}$ | Depth of the unsaturated zone |
| $z_{sat}$ | Depth of the saturated zone |
| $z_{unsat}$ | Depth of the unsaturated zone |
| $\mathcal{P}_{\bar{m}}\{\cdot\}$ | PMF of $\bar{m}_a$ |
| $\bar{\bar{m}}$ | Database listing all records of $\bar{m}_a$ |
| $M$ | Number of variables listed in of $\bar{\bar{m}}$ |
| $f_{SB}$ | SB frequency |
| $X$ | Spatial dimension of $\bar{m}$ and $\bar{m}_a$ (*x*-axis) |
| $Y$ | Spatial dimension of $\bar{m}$ and $\bar{m}_a$ (*y*-axis) |
| $x$ | Spatial coordinate (*x*-axis) |
| $y$ | Spatial coordinate (y-axis) |
| $X$ | Spatial dimension of $\bar{m}$ and $\bar{m}_a$ (*x*-axis) |
| $Y$ | Spatial dimension of $\bar{m}$ and $\bar{m}_a$ (*y*-axis) |
| $t_0^a$ | Starting time of the atmospheric dispersion and deposition process |
| $T_a$ | Ending time of the atmospheric dispersion and deposition process |
| $T_g$ | Ending time of the groundwater contaminant transport |
| $x^*$ | Spatial coordinate of the area of interest (*x*-axis) |
| $y^*$ | Spatial coordinate of the area of interest (y-axis) |
| $X^*$ | Spatial dimension of the area of interest (*x*-axis) |
| $Y^*$ | Spatial dimension of the area of interest (*y*-axis) |
| $P_n\{\cdot\}$ | PMF of $n$ |

## 1. Introduction

A Probabilistic Safety Assessment (PSA) of a Nuclear Power Plant (NPP) is structured in three levels (IAEA, 2001, 2024): Level 1 (L1) comprises the analysis and screening of potential hazards (internal, i.e., due to failures of components and systems, and external, i.e., due to natural events like flooding and earthquakes), the estimation of the frequency of the accident Initiating Events (IEs) and the evaluation of the accident sequences, in terms of Plant Damage States (PDSs) and Core Damage Frequency (CDF); this is typically done by combining Fault Trees (FTs), Event Trees (ETs) and numerical simulations (Baek and Heo, 2023); Level 2 analyses the accident physical progression in the NPP containment building for each PDS to determine the amount and timing of the Source Term (ST) of radionuclide release outside the NPP, i.e., the Source Term Categories (STCs); Level 3 evaluates the off-site consequences from the evolution of the accidents by considering the short and long-term effects of the release of each STC, evaluating the dose to population (Ali and Kakosimos, 2023; Park *et al.*, 2025), the environmental contamination (Selivanova *et al.*, 2025), the economic losses (Ashley *et al.*, 2017).

The outcomes of PSA are used for risk-informed decision making on NPP design and siting (L1 PSA), severe accident management (L2 PSA) (Roma, Di Maio and Zio, 2024) and evacuation procedures (L3 PSA) (Kim and Heo, 2023). In particular, L3 PSA outcomes provide risk information to regulators, politicians and the population at large, for an objective assessment of the impact of nuclear accidents (Denning and Mubayi, 2017; Selivanova *et al.*, 2025). Inevitably, PSA outcomes are affected by uncertainties due to modelling simplifications, necessary to reduce the complexity of the analysis, and incomplete knowledge of the phenomena involved in the accidents development (Mosleh, 2014; Ilkka, 2018).

Climate Change (CC) can affect the safety of NPPs in various ways (OECD, 2021; Yan, Dunnett and Andrews, 2023). On one hand, it can increase the frequency and magnitude of natural events (Seneviratne *et al.*, 2012; Utsumi and Kim, 2022), e.g., floodings (Tolo, Patelli and Beer, 2017; Kim, Kim, Hahm and Han, 2021a; Kim, Kim, Hahm, Park, *et al.*, 2021), typhoons (Kim, Jang and Lim, 2015; Choun and Kim, 2019; Kim *et al.*, 2024a, 2025) and tsunamis (Kim and Choi, 2012; Kim, Song and Cho, 2022), that can trigger external Initiating Events (IEs) like Station Blackouts (SBs) (Kim, 2022; Ayoub and Sornette, 2023; Yoon, Kim and Han, 2024; Vododokhov, Erlandson and Novog, 2025). On the other hand, it can affect the processes of dispersion, deposition and migration of radionuclides (Kitamura *et al.*, 2015; Biwalkar *et al.*, 2023), e.g., changing the

infiltration fluxes and aquifer recharge magnitudes in the contaminated region (Meray et al. 2024; Libera et al. 2019). To the authors knowledge, PSA frameworks do not comprehensively account for the effects of CC. Meteorological data variability has been accounted for, but only for fallout modelling in (An *et al.*, 2016), for the evaluation of short-term dose to the population (Sinha, Atikler and Mileski, 2024) and for the optimization of evacuation procedures (Kim and Heo, 2023).

Within this paper, a modelling and simulation framework is proposed to evaluate the effects of CC on groundwater radioactive contamination. The effects are considered in terms of modifications of the IE frequencies within L1 PSA, due to the increase of the frequency of extreme natural events and to changes in the hydrological conditions affecting aquifer radioactive contamination (Coscia, Di Maio and Zio, 2025). The PSA modelling and simulation framework integrates:

*i)* a CC impact assessment model based on Global Circulation Models (GCMs) developed within the Coupled Model Intercomparison Project Phase 6 (CMIP6) (Shin *et al.*, 2021) that allows calculating projections in the future of relevant CC variables,

*ii)* L1 and L2 PSA models to estimate the released ST (Lee and Ko, 2008; Oh *et al.*, 2020),

*iii)* an atmospheric dispersion model (Hybrid Single-Particle Lagrangian Integrated Trajectory model (HYSPLIT)) (Rolph, Stein and Stunder, 2017) to assess the contaminant deposition on the ground,

*iv)* a groundwater contaminant transport model (GoldSim) (Lee and Choi, 2016) to evaluate the aquifer contamination.

Coupled Monte Carlo simulation is used for the propagation of the major sources of uncertainties affecting the assessment, including the magnitude of the emitted ST, the meteorological conditions for atmospheric dispersion, and the climatic and physical parameters affecting contaminant transport through groundwater. The developed framework is applied to a case study regarding a hypothetical severe accident in a NPP site located in South Korea, and its consequences are evaluated on two aquifers located nearby the NPP (one confined and one unconfined). The modelling and simulation framework proposed provides also for a bounding analysis of the peak yearly dose from groundwater ingestion, considering a set of baseline accident scenarios that initiate at the current time and in which the groundwater contamination develops under both stationary and CC-modified climatic conditions, and other scenarios representative of the same accident but assumed to be initiated in 2100 and developing under CC-induced climatic conditions. The choice of these

two categories of scenarios is instrumental to assess the effects that CC could have on the results of the PSA of newly built NPPs (with sixty years of design operative license, plus twenty years life extension) considering that accidents may occur at the beginning or towards the end of the NPP design lifetime. The results of the case study show that under the assumptions made for the considered nuclear accident, CC influences groundwater radioactive contamination thus, possibly, worsening the exceedance of the annual dose limit from the ingestion of contaminated groundwater. Clearly, an ad-hoc comprehensive hazard and fragility analysis would be required for evaluating site-specific CC impacts.

The paper is organized as follows: Section 2 presents the proposed PSA framework, Section 3 presents the case study, Section 4 presents the results and in Section 5 conclusions are drawn.

## 2. The proposed PSA framework

A sketch of the proposed simulation-based PSA framework is presented in Figure 1.

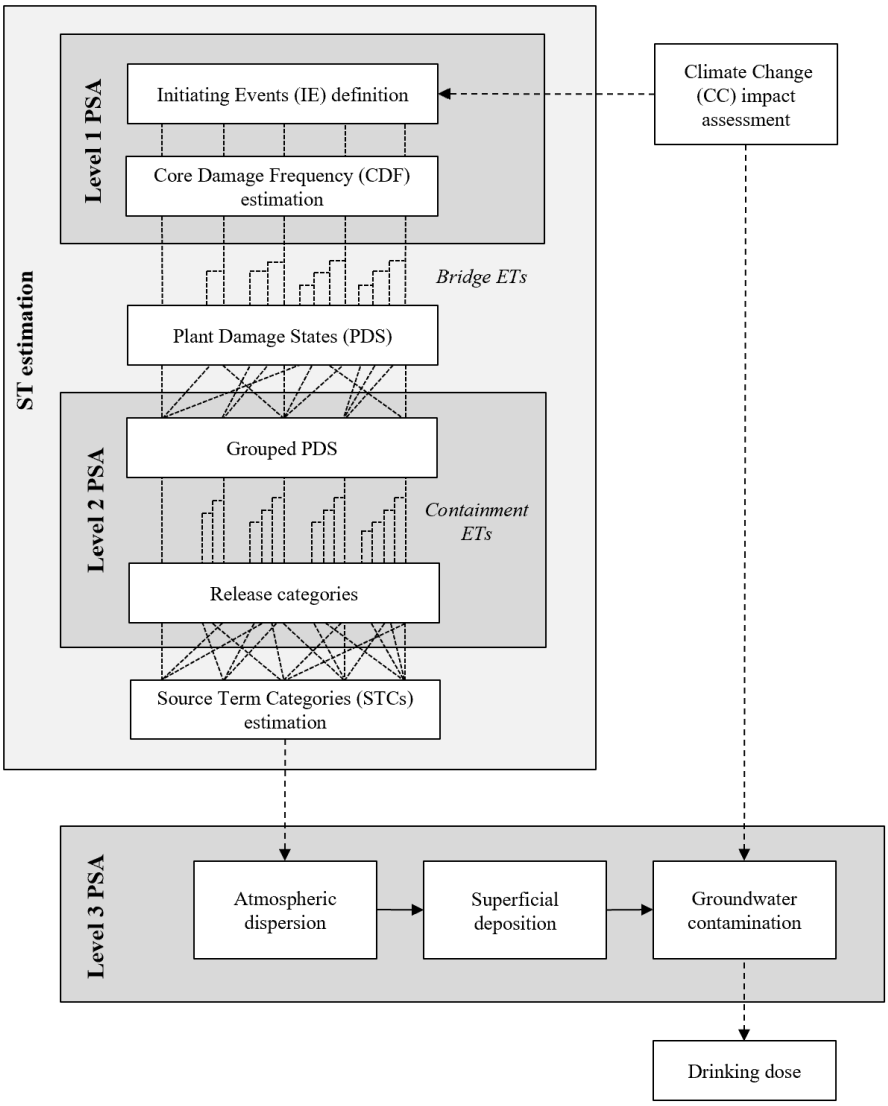


**Figure 1.** Simulation-based PSA framework.

The framework allows calculating the peak yearly drinking dose from contaminated groundwater ingestion by combining four models: *i*) a CC impact assessment model (Section 2.1), *ii*) a ST estimation model comprising L1-L2 PSA models (Section 2.2), *iii*) an atmospheric dispersion and deposition model (Section 2.3), and *iv*) a groundwater contaminant transport model (Section 2.4). The coupling between the four models is performed through a Monte Carlo simulation scheme for propagating uncertainty (Section 2.5). The overall framework can allow accounting for CC effects within a standard PSA framework (IAEA, 2001, 2024).

## 2.1 CC impact assessment model

For the projections of future climatic conditions due to CC in a region of interest, models are developed and the corresponding numerical codes are built to simulate the future dynamics of $M$ climatic variables, such as temperature, precipitation and sea level. Let $\bar{m}(x, y, t)$ denote the vector of values of the $M$ climatic variables at time $t$ in the location of spatial coordinates $(x, y)$, with $x = 1, 2, \dots, X$, $y = 1, 2, \dots, Y$, and $t = t_0, \dots, T$, $t_0$ being the current time and $T$ the time of interest for the projection. The climate dynamics can be simulated under different assumptions regarding anthropogenic and natural forcings, such as greenhouse gas emissions, land use changes and solar activity that, in turn, are linked to economic growth, demography and policy interventions (O'Neill *et al.*, 2016), collectively named Shared Socioeconomic Pathways (SSPs). Among others (McGuffie and Henderson-Sellers, 2001; Edwards, 2011), GCMs are those considered by the international initiative Coupled Model Intercomparison Project Phase 6 (CMIP6) (Shin et al. 2021;Tebaldi et al. 2021) which organises different GCMs, input data, documentation and evaluation metrics in a common experimental framework to derive a multi-models ensemble of GCMs useful to compare the effects of the different SSPs on variables such as temperature, precipitation, sea-level rise projections, which ultimately affect the frequency of natural extreme events, e.g., floodings due to extreme precipitation (B. J. Kim, Kim, Hahm, and Han 2021), tsunamis due to sea level rise (Yavuz, 2023), forest fires due to heat waves (Lim et al. 2024) and tropical cyclones due to the combined effect of wind speed and precipitation intensification (Gungyu Kim et al. 2024). Then, a CC-induced increase can be expected also of the frequencies $f_i(T)$ of the external IEs, $i = 1, 2, \dots, I$, at the future time $T$ (OECD, 2021; Di Maio, Tonicello and Zio, 2022):

$$f_i(T) = \alpha_i \, f_i(t_0) \tag{1}$$

where, under the hypotheses that *i*) the $i$-th IE is affected by the variation of a single climatic variable $m(x, y, t)$ and that *ii*) the fragility of the NPP Structures, Systems and Components (SSCs) is time invariant, the increase multiplication factor $\alpha_i$ is:

$$\alpha_i = 1 + \varepsilon_i \left( m(x, y, T) - m(x, y, t_0) \right) \tag{2}$$

where $\varepsilon_i$ depends on the fragility curve related with the $i$-th IE and on $m(x, y, t_0)$ (further details can be found in Appendix A).

CC may also alter the hydrological balance of the region of interest, i.e., the infiltration (or recharge) flux of the contaminated aquifers, which is hereafter denoted as the aquifer Climatic Boundary Condition (CBC) (Kim *et al.*, 2020; Song *et al.*, 2021; Song, Chung and Shahid, 2022). Changes in aquifer CBC may increase or decrease the mobility of the radionuclides released in groundwater and, therefore, the magnitude of the environmental consequences of the accident, depending on whether precipitation or evapotranspiration dominates (wet and dry scenarios, respectively). To account for this, an additive factor of change $\beta$ for the aquifer CBC is considered, as in (Libera *et al.*, 2019; la Cecilia *et al.*, 2020):

$$\beta = \frac{\dot{\psi}(T) - \dot{\psi}(t_0)}{\dot{\psi}(t_0)} \tag{3}$$

where the infiltration flux in the future $\dot{\psi}(T)$ and the current infiltration flux $\dot{\psi}(t_0)$ are estimated assuming that the climatic variables (e.g., precipitation and temperature) at time $T$ and $t_0$ for the location $(x, y)$ are equal to $\bar{m}(x, y, T)$ and $\bar{m}(x, y, t_0)$, respectively.

Note that since the magnitude of $\alpha_i$, $i = 1,2, \dots, I$ and $\beta$ are related to the climatology and topography of the region where the NPP is located, they depend on the considered SSP and GCMs.

### 2.2 ST estimation model (L1-L2 PSA)

L1 and L2 PSA are, then, performed to estimate $J$ STCs, their frequencies of release $f^j$, $j = 1,2, \dots, J$ and the corresponding Release Fraction (RF) $\bar{R}^j = \left[R_1^j, \dots, R_r^j, \dots, R_R^j\right]$, where $r = 1, 2, \dots, R$ are the different radionuclide species considered. The released ST is obtained by the product of the RF and the core inventory at the time of the accident occurrence $t_0^a$.

### 2.3 Atmospheric dispersion and deposition model (L3 PSA)

An atmospheric dispersion and deposition model is used to estimate the concentration of radionuclides deposited at a given distance from the ST release. To do this, different models are available in literature: to name a few, under the simplifying assumptions of stationarity, e.g., time invariant wind fields and constant ST emission rate, the analytical gaussian plume can be adopted (Lotrecchiano *et al.*, 2020); when non-stationary meteorological variables and ST sources are instead considered, the Advection Dispersion Equation (ADE) model can be used, following a Eulerian or a Lagrangian approach (Challa *et al.*, 2008). In this work, an ADE model is employed to consider the effect of non-stationary meteorological variables $\overline{m}_a(x, y, t)$ in a time interval $t \in [t_0^a, T_a]$.

It is worth mentioning that since $[t_0^a, T_a] \ll [t_o, T]$, the meteorological variables values $\overline{m}_a(x, y, t)$ required for the simulation of the atmospheric dispersion and deposition processes, e.g., wind speed, wind direction, atmospheric pressure, relative humidity, temperature and precipitation, are not considered to be exposed to CC-induced variations; rather aleatory uncertainty becomes important. To quantify this, as in (Lim *et al.*, 2024), $N_m$ stochastic realizations of $\overline{m}_a(x, y, t)$ are collected, i.e., $\widehat{\overline{m}}(x, y, t) = \left[\overline{m}_a^{\,1}(\cdot), \dots, \overline{m}_a^{\,N_m}(\cdot)\right]$, and propagated through the model by assuming a site-specific Probability Mass Function (PMF) $\mathcal{P}_m$ (An *et al.*, 2016), e.g., a uniform PMF $\overline{m}_a(\cdot) \sim \mathcal{U}\{1, N_m\}$.

### 2.4 Groundwater contaminant transport model (L3 PSA)

A groundwater contaminant transport model is used to compute the concentration $C_r(t)$ of each $r$-th radionuclide at the end of the migration pathway ($t > T_a$). The CBC of the model is an imposed infiltration flux $\dot{\psi}(t)$:

$$\dot{\psi}(t) = \dot{\psi}(t_0) + \left(\beta\, \dot{\psi}(t_0)\right) \tag{4}$$

where $\dot{\psi}(t_0)$ is defined as:

$$\dot{\psi}(t_0) = \dot{P}(t_0) + \dot{Ir}(t_0) - \dot{ET}(t_0) - \dot{R}(t_0) \tag{5}$$

and $\dot{P}(t_0)$, $\dot{Ir}(t_0)$, $\dot{ET}(t_0)$, $\dot{R}(t_0)$ are a random realization of precipitation, irrigation, evapotranspiration and runoff fluxes estimated under the current climatic conditions $\overline{m}(x, y, t_0)$.

Then, the total dose $D(t)$ is calculated as:

$$D(t) = \sum_{r=1}^{R} C_r(t)\ DC_r\ V_w \tag{6}$$

where $DC_r$ is the dose conversion factor of each $r$-th radionuclide species and $V_w$ the total volume of water consumed by an adult in one year. The total peak dose $D_{peak}$ is obtained as in Eq. 7:

$$D_{peak} = \max_{t\,\in\,[T_a, T_g]} D(t) \tag{7}$$

Then, the breakthrough time $t_{peak}$, i.e., the time corresponding to $D_{peak}$, is:

$$t_{peak} = \operatorname*{argmax}_{t\,\in\,[T_a, T_g]} D(t) \tag{8}$$

where $t \in [T_a, T_g]$ refers to the time interval considered for the groundwater contaminant transport.

### 2.5 Monte Carlo simulation

The coupling of the ST estimation model (Section 2.2), the atmospheric dispersion model (Section 2.3) and the groundwater contaminant transport model (Section 2.4) is performed through the Monte Carlo simulation scheme sketched in Figure 2. The framework is composed by two loops: one to estimate with $N_s$ trials (indexed by $s$) the deposited ST and the other to estimate with $N_g$ trials (indexed by $g$) the peak dose from groundwater ingestion. The simulation starts by setting the CC impact parameters $\alpha_i$, $i = 1,2, \dots, I$, and $\beta$, for each $s$-th trial of the first loop the released ST is estimated as customary done by L1-L2 PSA, also, the case of a multi-unit NPP can be addressed by modelling the number of units $n = 1, 2, \dots, N$, that are simultaneously affected by the accident with a Probability Mass Function (PMF) $P_n$ (for the sake of simplicity here assumed the same for all the IEs) (Lim, Han and Yang, 2016; Yang, 2018). The atmospheric dispersion model is run with the random

meteorological variables $\bar{m}_a(x,y,t)$ sampled from $\mathcal{P}_m\{\widehat{\bar{m}}(\cdot)\}$, to calculate the deposited ST. After $N_s$ trials, a Probability Density Function (PDF) of the deposited ST can be obtained (GoldSim 2021b; Iman and Conover 1982). At this point, for each $g$-th trial of the second loop, the groundwater contaminant transport model is to be run, fed with a value of random CBC. After $N_g$ trials, the PDFs c are estimated.

It is worth noting that, the two loop Monte Carlo simulation scheme allows setting $N_s \gg N_g$, so as to address the issue of the estimation of the peak dose for which the physical model of groundwater contaminant transport is more computationally expensive than the atmospheric dispersion model used to estimate the deposited ST. The representativeness of the estimated $D_{peak}$ and $t_{peak}$ PDFs is ensured by implementing an importance-sampling algorithm, which enables the simulation of physically consistent scenarios of large deposited ST. Indeed, the induced rank-correlation method (Iman and Conover 1982) has been applied to preserve the correlation coefficients among the marginal samples of the various deposited radionuclide species.

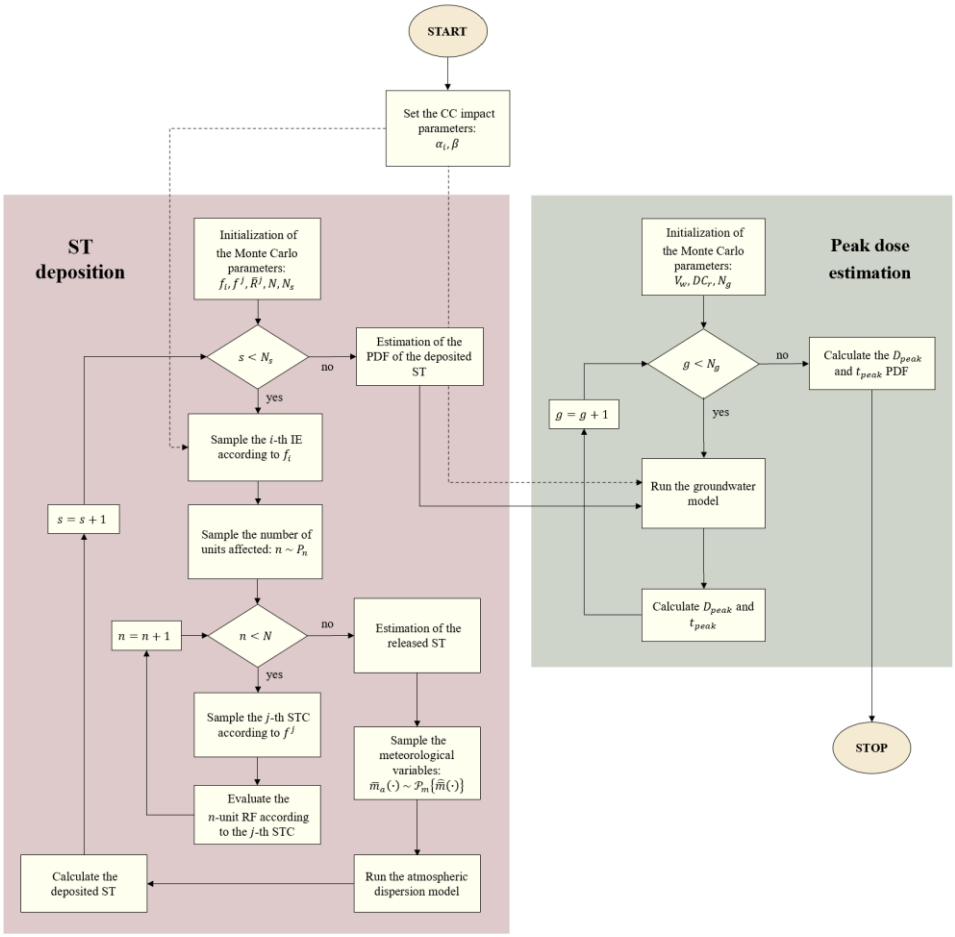


**Figure 2.** Flowchart of the proposed Monte Carlo simulation scheme, that couples: *i*) CC projections for the determination of $\alpha_i$ and $\beta$ *ii*) L1-L2 PSA for the determination of $f_i$ and STCs *iii*) an atmospheric dispersion

model for the deposited ST estimation *iv*) a contaminant transport model for the estimation of the peak dose from the ingestion of contaminated groundwater.

## 3. Case Study: CC-impact on the groundwater radioactive contamination from a multi-unit NPP

The PSA framework is applied to a $N = 6$ units NPP located in a hypothetical region in South Korea ($x^* = x_0^*, x_1^*, \dots, X^*, y^* = y_0^*, y_1^*, \dots, Y^*$), shown in Figure 3 (square marker). The aquifers whose groundwater ingestion dose peak is calculated are $A_1$ and $A_2$ (circle and triangle, respectively). The aquifers have different hydrogeological characteristics, i.e., $A_1$ is a confined aquifer underlaying reclaimed floodplains (Kim *et al.*, 2006) whereas $A_2$ is a shallow costal unconfined aquifer (Lee and Song, 2007). For both aquifers the same principal groundwater direction remains east-west, extending from the inland mountains towards the seashore (Kim *et al.*, 2019) (more details can be found in Section 3.4.1 and Section 3.4.2, respectively).

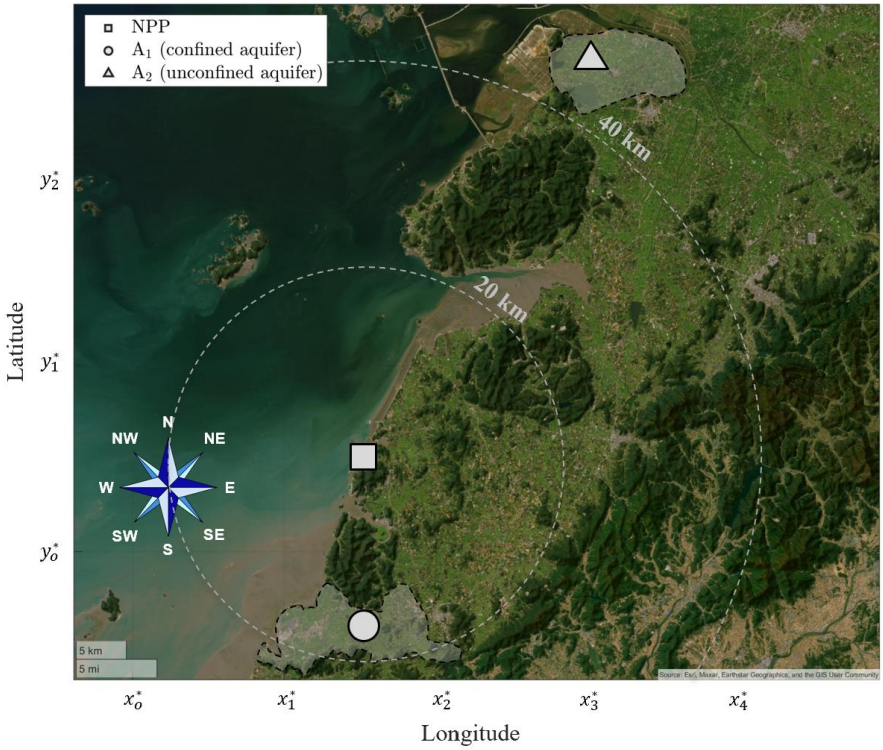


**Figure 3.** Case study aerial view.

### 3.1 CC impact assessment model

CMIP6 simulations, under different SSPs, predict an increase of mean, variance and extreme values of climatic variables, especially temperature and precipitation, due to CC in South Korea (Y. H. Kim et al. 2020; Song, Chung, and Shahid 2022). This is expected to lead to increased frequency and intensity of heavy rainfall and prolonged droughts (Shin et al. 2021; CCKP 2025), so that is not sure whether South Korea will predominantly face wetter or drier conditions. For this reason, we consider two scenarios sets:

*i)* *Baseline*: the accident is supposed to occur at the beginning of the lifetime of a newly built NPP, thus with no CC-induced increase of the frequency of extreme natural events. On the other hand, the groundwater contamination process could still be affected by CC-driven alterations of CBCs, e.g., decrease, stationary or increase of the aquifer infiltration rate. Then, we consider the scenarios $Baseline_{Dry}$, $Baseline_{Stationary}$, and $Baseline_{Wet}$, respectively.

*ii)* *CC-induced*: the accident is supposed to occur towards the end of the lifetime of a newly built NPP, therefore a CC-induced increase of the frequency of extreme precipitation events is expected to occur and lead to an increase of the IEs frequencies. Also in this case, drier, stationary or wetter CBC are considered, namely $CC\text{-}induced_{Dry}$, $CC\text{-}induced_{Stationary}$, and $CC\text{-}induced_{Wet}$, scenarios.

The IEs considered in the analysis are Steam Generator Tube Rupture (SGTR), Loss of Coolant Accident (LOCA) and Station Blackout (SB). Among these, we consider that only SB might be impacted by an intensification of extreme precipitation events due to CC, so that $\alpha_{SGTR} = \alpha_{LOCA} = 1$ for all the CC scenarios. In particular, a SB resulting from the simultaneous loss of off-site power and failure of emergency core-cooling systems can be triggered by a flooding that disables both the external grid supplying the NPP and the on-site diesel generators and auxiliary battery packs (Yoon, Kim and Han, 2024), whereas SGTR and LOCA, although initiated by natural hazards, are not further aggravated by CC-induced variations of climatic variables. The CC scenarios are outlined in Table 1 and their effects on L1 and L3 PSA are operationalized as follows:

- L1 PSA:
  - *Baseline*: no increase of the baseline SB frequency $f_{SB}$ is assumed, i.e., $\alpha_{SB} = 1$.

- *CC-induced*: a ten-fold increase of $f_{SB}$ is assumed, i.e., $\alpha_{SB} = 10$ at $T = 2100$. This value results from the variation of extreme daily precipitation (with a 50 yr return period) taken from the CMIP6 SSP5-8.5 projections for the years 2071-2100 with respect to the historical records relative to the years 1973-2010 (Shin et al. 2021), i.e., 44 %, and from the multiplication by $\varepsilon_{SB} = 0.095$ (see Appendix B for details).

- L3 PSA:
  - *Dry*: a maximum 25 % decrease ($\beta = -25\,\%$) of aquifer infiltration flux $\dot{\psi}(t)$ is assumed to reflect the reduction of $\dot{P}$ and the increase of $\dot{ET}$ according to CMIP6 SSP5-8.5 projections for the region of interest in the years 2080-2100 (Kim *et al.*, 2020; Shin *et al.*, 2021; Song *et al.*, 2021; Song, Chung and Shahid, 2022; CCKP, 2025) with respect to the historical records relative to the 1960-2020 years (KMA, 2025). For the sake of simplicity, variations of irrigation and runoff fluxes of Eq. 5 are neglected.

  - *Stationary*: no variation of the aquifer infiltration flux is considered, assuming that changes in $\dot{P}$ and $\dot{ET}$ balance each other.

  - *Wet*: a maximum 25 % increase ($\beta = +25\,\%$) of aquifer infiltration flux $\dot{\psi}(t)$ is assumed to reflect the increase of $\dot{P}$ and the decrease of $\dot{ET}$ according to CMIP6 SSP5-8.5 projections for the region of interest for the years 2080-2100 (Kim *et al.*, 2020; Shin *et al.*, 2021; Song *et al.*, 2021; Song, Chung and Shahid, 2022; CCKP, 2025) with respect to the historical records relative to the 1960-2020 years (KMA, 2025). Also in this case, variations of irrigation and runoff fluxes are neglected (Eq. 5).

| **Scenario** | **Explanation** | **Label** | **CC assumptions** | **Effect on L1** | **Effect on L3** |
|---|---|---|---|---|---|
| Baseline | Accident occurring at $t_0$ | $Baseline_{Dry}$ | No modifications of $f_{SB}^{hist}$; drier climatic conditions $(\dot{P} < \dot{ET})$ | $\alpha_{SB} = 1$ | $\beta = -25\,\%$ |
| | | $Baseline_{Stationary}$ | No CC-induced effects | $\alpha_{SB} = 1$ | $\beta = 0$ |

| | | | | | |
|---|---|---|---|---|---|
| CC-induced | Accident occurring at the end of the NPP lifetime $T$ | $Baseline_{Wet}$ | No modifications of $f_{SB}^{hist}$; wetter climatic conditions $(\dot{P} > \dot{E}T)$ | $\alpha_{SB} = 1$ | $\beta = +25\ \%$ |
| | | $CC\text{-}induced_{Dry}$ | Increase of $f_{SB}^{hist}$; drier climatic conditions $(\dot{P} < \dot{E}T)$ | $\alpha_{SB} = 10$ | $\beta = -25\ \%$ |
| | | $CC\text{-}induced_{Stationary}$ | Increase of $f_{SB}^{hist}$; stationary climatic conditions | $\alpha_{SB} = 10$ | $\beta = 0$ |
| | | $CC\text{-}induced_{Wet}$ | Increase of $f_{SB}^{hist}$; wetter climatic conditions $(\dot{P} > \dot{E}T)$ | $\alpha_{SB} = 10$ | $\beta = +25\ \%$ |

**Table 1.** List of the considered CC scenarios.

### 3.2 ST estimation model

The IEs frequencies $f_i(t_0)$ are listed in Table 2 (U.S. Nuclear Regulatory Commission, 1996). Among the $N$ NPP units, the probability that $n$ of them are simultaneously affected by the accident is modelled by a truncated discrete exponential PMF (Berber, 2017):

$$P_n = \frac{e^{\lambda} - 1}{1 - e^{-\lambda N}}\, e^{-\lambda n} \tag{9}$$

with $\lambda = 0.2$ for all IEs (Lim, Han and Yang, 2016; Yang, 2018). This assumption is instrumental to the exemplification of the framework on a multi-unit NPP: clearly, this can be replaced by site and IEs specific PMFs (see Appendix C for further details). A total of $J = 14$ STCs are considered (Lee and Ko, 2008); for each generic $j$-th STC, Table 3 lists the possible IEs that might cause it, the corresponding frequency of release $f^j$, and the RFs $R^j(^{90}\mathrm{Sr})$ and $R^j(^{137}\mathrm{Cs})$ of the two radionuclides $^{137}$Cs and $^{90}$Sr considered responsible for groundwater contamination. The considered inventory of these radionuclides at the release time refers to that of a generic 1000 MWe light water reactor with 33% thermal efficiency at the end of the irradiation cycle, a core capacity of 70 metric tonnes of fresh fuel (tonU) and a burnup level of 45 GWd/tonU (U.S. Nuclear Regulatory Commission, 2016).

| IE | $f_i(t_0)$ [yr$^{-1}$] | Source |
|---|---|---|
| SGTR | $7 \cdot 10^{-4}$ | (U.S. Nuclear Regulatory Commission, 1996) |
| LOCA | $1 \cdot 10^{-6}$ | (U.S. Nuclear Regulatory Commission, 2005) |

| | | |
|---|---|---|
| SB | $1 \cdot 10^{-5}$ | (U.S. Nuclear Regulatory Commission, 1996) |

**Table 2.** List of IEs and of the frequencies of occurrence $f_i$.

| STC | IE | Characteristics of the accident | $f^j$ [yr$^{-1}$] | $R^j$($^{90}$Sr) [-] | $R^j$($^{137}$Cs) [-] |
|---|---|---|---|---|---|
| $STC_1$ | SB/LOCA | RPV intact and functioning containment isolation | $1 \cdot 10^{-6}$ | $4.7 \cdot 10^{-6}$ | $1.8 \cdot 10^{-5}$ |
| $STC_2$ | SB/LOCA | RPV intact and loss of containment isolation | $1 \cdot 10^{-12}$ | $6.7 \cdot 10^{-3}$ | $2.9 \cdot 10^{-1}$ |
| $STC_3$ | LOCA | Containment failure before RPV breach | $8.2 \cdot 10^{-8}$ | $7.5 \cdot 10^{-5}$ | $1 \cdot 10^{-5}$ |
| $STC_4$ | SB | Containment early failure (RPV breaches under high pressure with sprays available) | $3.7 \cdot 10^{-9}$ | $2.2 \cdot 10^{-3}$ | $1.1 \cdot 10^{-2}$ |
| $STC_5$ | SB | Containment early failure (RPV breaches under high pressure with sprays unavailable) | $1.6 \cdot 10^{-8}$ | $6.2 \cdot 10^{-4}$ | $1.5 \cdot 10^{-2}$ |
| $STC_6$ | SB/LOCA | Containment early failure (RPV breaches under low pressure with sprays unavailable) | $7.2 \cdot 10^{-8}$ | $8.6 \cdot 10^{-3}$ | $1.6 \cdot 10^{-1}$ |
| $STC_7$ | LOCA | Containment late failure (sprays available) | $8 \cdot 10^{-7}$ | $5.3 \cdot 10^{-6}$ | $2.2 \cdot 10^{-5}$ |
| $STC_8$ | SB | Containment late failure (sprays unavailable) | $1.4 \cdot 10^{-6}$ | $2.9 \cdot 10^{-5}$ | $4.1 \cdot 10^{-4}$ |
| $STC_9$ | SB/LOCA | Basement melt-through (sprays unavailable) | $2.2 \cdot 10^{-6}$ | $3 \cdot 10^{-6}$ | $4.6 \cdot 10^{-5}$ |
| $STC_{10}$ | SB/LOCA | Containment intact | $3.3 \cdot 10^{-7}$ | $3 \cdot 10^{-6}$ | $4.6 \cdot 10^{-5}$ |
| $STC_{11}$ | SB/LOCA | RPV breaches (sprays available) | $1 \cdot 10^{-12}$ | $7.7 \cdot 10^{-3}$ | $1.8 \cdot 10^{-2}$ |
| $STC_{12}$ | SB/LOCA | RPV breaches (sprays unavailable) | $1 \cdot 10^{-12}$ | $8.1 \cdot 10^{-3}$ | $2.1 \cdot 10^{-1}$ |
| $STC_{13}$ | SGTR | Steam Generator Tube Rupture | $1.3 \cdot 10^{-6}$ | $8.6 \cdot 10^{-5}$ | $1.2 \cdot 10^{-2}$ |
| $STC_{14}$ | LOCA | Interface LOCA | $2.5 \cdot 10^{-8}$ | $1.1 \cdot 10^{-1}$ | $9.9 \cdot 10^{-1}$ |

**Table 3.** STCs with corresponding IE, characteristics, frequency, RF of $^{90}$Sr and $^{137}$Cs (Lee and Ko, 2008) (SB: Station Blackout; LOCA: Loss of Coolant Accident; SGTR: Steam Generator Tube Rupture; RPV: Reactor Pressure Vessel).

### 3.3 Atmospheric dispersion and deposition model

The HYbrid Single-Particle Lagrangian Integrated Trajectory (HYSPLIT) model is used for describing radionuclides atmospheric dispersion and deposition following an accident (Draxler and Hess 1997; Rolph, Stein, and Stunder 2017). HYSPLIT uses the parameters listed in Table 4 and the dispersion-relevant meteorological parameters $\bar{m}_a(x, y, t)$ (wind speed, wind direction, atmospheric pressure, relative humidity, temperature, precipitation) to model the contaminant dispersion and deposition. In this work, the month of July is chosen as conservatively representative of the regional meteorology, since the prevalent wind directions are from south-west to north-east: considering the region topography (Figure 3), under these meteorological conditions the inland transport of radionuclides is maximum. The time interval $[t_0^a, T_a]$ considered for the dispersion and deposition processes is 72 hours. To account for the uncertainty related to $\bar{m}_a(x, y, t)$, all the available $N_m = 104$ different realizations of the meteorological variables over the 72 hours length records are retrieved from the GDAS-0.5° database $\hat{\bar{m}}(\cdot)$ relative to the month of July in the years 2007-2019 (NOAA, 2024) ($\bar{m}_a(\cdot) \sim \mathcal{U}\{1, N_m\}$).

| Parameter | Value | Unit | Source |
|---|---|---|---|
| Emission height | 50 | $m$ | Engineering judgement |
| Dry deposition velocity | $2 \cdot 10^{-3}$ | $m\,s^{-1}$ | (An *et al.*, 2016) |
| In-cloud scavenging coefficient | $3 \cdot 10^{-5}$ | $s^{-1}$ | (Kinser, 2001) |
| Below-cloud scavenging coefficient | $5 \cdot 10^{-5}$ | $s^{-1}$ | (An *et al.*, 2016) |
| Release duration | 8 | $hours$ | Engineering judgement |
| Simulation duration | 72 | $hours$ | Engineering judgement |

**Table 4.** List of the parameters of the HYSPLIT model.

### 3.4 Groundwater contaminant transport model

GoldSim is used to model groundwater contaminant transport, adopting a one-dimensional ADE to describe the most representative migration pathway for evaluating the peak dose $D_{peak}$ (Kowe and Norris 2012; GoldSim 2021a). This allows performing a large number of simulations in a reasonable computational time while considering the most influential phenomena affecting the contaminant migration through groundwater,

specifically, the retarding effect of sorption reactions between the radionuclides and the porous matrix, the radioactive decay and the effect of the time-dependent CBC $\dot{\psi}(t)$. The concentrations at the end of the pathway, i.e., the spatial position chosen as representative of a compliance well, are calculated with a daily time step, and $D_{peak}$ is calculated in the time interval $[T_a, T_g] = 100$ years through a user-defined receptor element (Lee and Choi, 2016). Details on the GoldSim models of the aquifers located in $A_1$ and $A_2$ are hereafter presented in Section 3.4.1 and Section 3.4.2, respectively.

### 3.4.1 $A_1$ groundwater contaminant transport model

$A_1$ is a floodplain region resulting from an anthropogenic process of land reclamation from the seashore to increase the surface of exploitable land for agricultural activities (Kim *et al.*, 2006). The reclamation process has caused the accumulation of a thick layer of muddy soil on the original sandy shore, creating a confined aquifer structure. A conceptual model of the aquifer structure is presented in Figure 4.

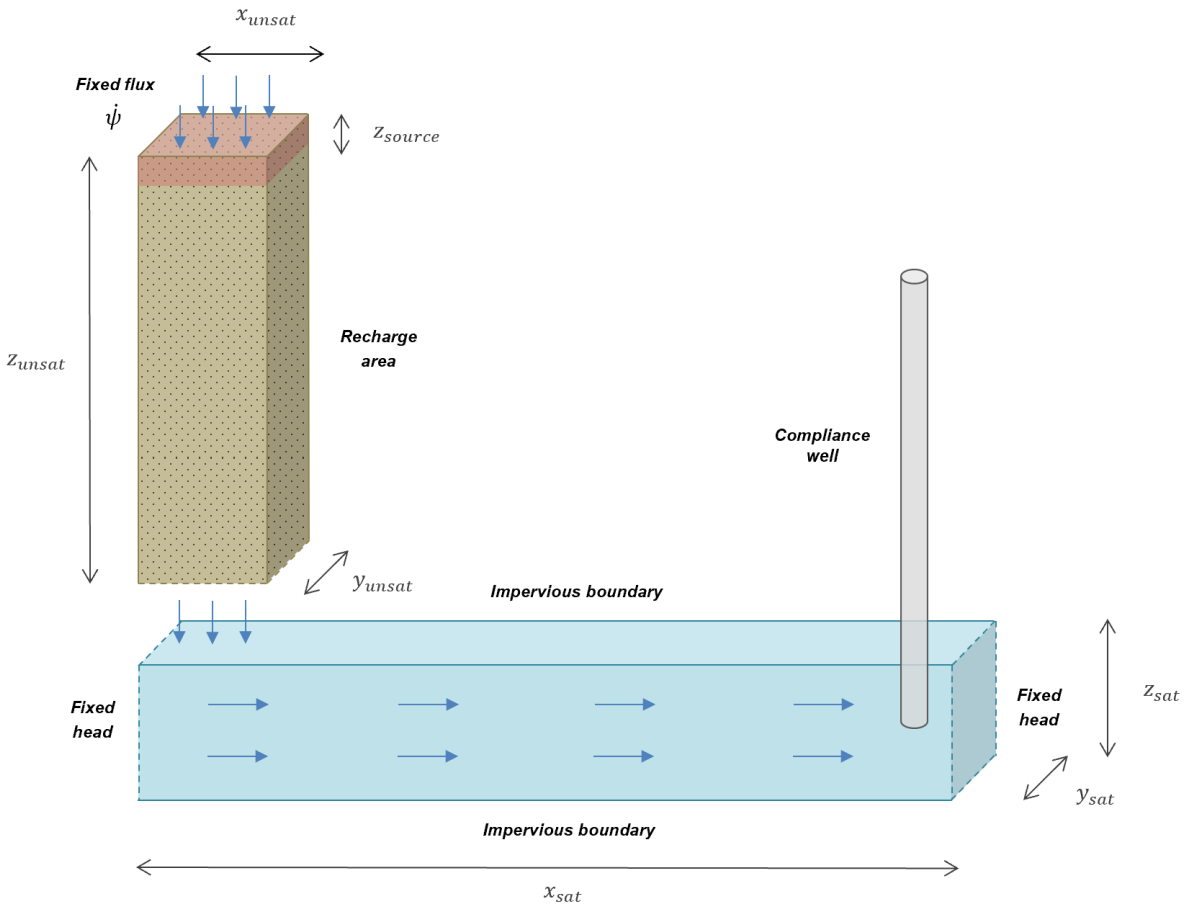

**Figure 4.** Conceptual model of the aquifer structure of $A_1$.

A representative radionuclide migration pathway for modelling the $A_1$ aquifer structure is built by connecting a vertical pipe element, representing a sandy unsaturated recharge area at the foothills of the north-eastern mountains (Figure 3), with a horizontal aquifer element representing the confined aquifer underlaying the floodplain. The contaminant source and the CBC $\dot{\psi}(t)$ are placed at the upper boundary of the recharge area due to the confined structure of the aquifer, and the compliance well is hypothesized to be at a $x_{sat}$ distance downgradient with respect to the recharge area. The flow in the horizontal aquifer is assumed to remain in steady state conditions for the whole duration of the process of groundwater contaminant transport and it is obtained through Darcy law as:

$$Q_{sat} = -K_{sat}\, A_{sat}\, \nabla h \tag{10}$$

where $K_{sat}$ is the saturated hydraulic conductivity, $A_{sat} = y_{sat}\, z_{sat}$ is the cross section of the pathway and $\nabla h$ is the hydraulic gradient. The geometrical and physical parameters of the developed groundwater model for $A_1$ are listed in Table 5. In particular, the distributions of $K_d$ and $\dot{\psi}(t_0)$ used in the $g$-th loop of Monte Carlo simulation are provided; specifically, for each $g$-th trial, $\dot{\psi}(t_0)$ is resampled at each simulation time step to describe the daily fluctuations of the CBC $\dot{\psi}(t)$.

| Parameter | Symbol | Value | Unit | PDF | Source |
|---|---|---|---|---|---|
| Infiltration flux | $\dot{\psi}(t_0)$ | 2 | $mm\ day^{-1}\ m^{-2}$ | Exponential | (KIGAM, 1997; Kim *et al.*, 2006), (GIMS, 2025), Engineering judgement |
| Source depth | $z_{source}$ | 0.02 | $m$ | [−] | Engineering judgement |
| Unsaturated zone length | $x_{unsat}$ | 10 | $m$ | [−] | Engineering judgement |
| Unsaturated zone thickness | $y_{unsat}$ | 1 | $m$ | [−] | Engineering judgement |
| Unsaturated zone depth | $z_{unsat}$ | 5 | $m$ | [−] | Engineering judgement |
| Unsaturated zone longitudinal dispersivity | $\alpha_{L,unsat}$ | 0.5 | $m$ | [−] | Engineering judgement |
| Unsaturated zone saturation level | $S_{l,unsat}$ | 0.6 | [−] | [−] | Engineering judgement |
| Saturated zone length | $x_{sat}$ | 100 | $m$ | [−] | Engineering judgement |
| Saturated zone thickness | $y_{sat}$ | 1 | $m$ | [−] | Engineering judgement |
| Saturated zone depth | $z_{sat}$ | 3 | $m$ | [−] | Engineering judgement |
| Distribution coefficient of $^{137}$Cs (sand) | $K_{d,^{137}Cs}^{sand}$ | $530 \pm 6$ | $l\ kg^{-1}$ | Gaussian | (Gil-García, Rigol and Vidal, 2009) |

| | | | | | |
|---|---|---|---|---|---|
| Distribution coefficient of $^{90}$Sr (sand) | $K_{d,^{90}Sr}^{sand}$ | $22 \pm 6$ | $l\,kg^{-1}$ | Gaussian | (Gil-García, Rigol and Vidal, 2009) |
| Saturated zone longitudinal dispersivity | $\alpha_{L,sat}$ | 10 | $m$ | [−] | Engineering judgement |
| Saturated zone saturation level | $S_{l,sat}$ | 1 | [−] | [−] | Engineering judgement |
| Saturated zone hydraulic conductivity | $K_{sat}$ | $10^{-4}$ | $m\,s^{-1}$ | [−] | (Kim *et al.*, 2006) |
| Hydraulic gradient | $\nabla h$ | 0.02 | [−] | [−] | (KIGAM, 1997) |
| $^{137}$Cs dose conversion factor (adult) | $DC_{^{137}Cs}$ | $1.3 \cdot 10^{-8}$ | $Sv\,Bq^{-1}$ | [−] | (ICRP, 2012) |
| $^{90}$Sr dose conversion factor (adult) | $DC_{^{90}Sr}$ | $2.8 \cdot 10^{-8}$ | $Sv\,Bq^{-1}$ | [−] | (ICRP, 2012) |
| Water consumption | $V_W$ | 730 | $l\,year^{-1}$ | [−] | (Cadini, Tosoni and Zio, 2016) |

**Table 5.** List of the parameters used for the GoldSim model of $A_1$.

### 3.4.2. $A_2$ groundwater contaminant transport model

$A_2$ is characterized by the presence of a shallow costal unconfined aquifer and presents a three-layered stratigraphy: a superficial loamy-sandy (70 % loam and 30 % sand) unsaturated layer which constitute the substrate for rice cultivations, an intermediate saturated sandy layer (the proper aquifer) and a semi-impermeable weathered granite bedrock (Lee and Song, 2007). Also in this case, the aquifer is modelled with GoldSim by connecting an unsaturated vertical pipe element with a horizontal aquifer element. To represent the unconfined structure, the deposited source and the infiltration flux CBC $\dot{\psi}(t)$ is applied along the whole extension of the pathway. A conceptual model of the $A_2$ aquifer structure is presented in Figure 5 and the related parameters and $\dot{\psi}(t_0)$ are listed in Table 6.

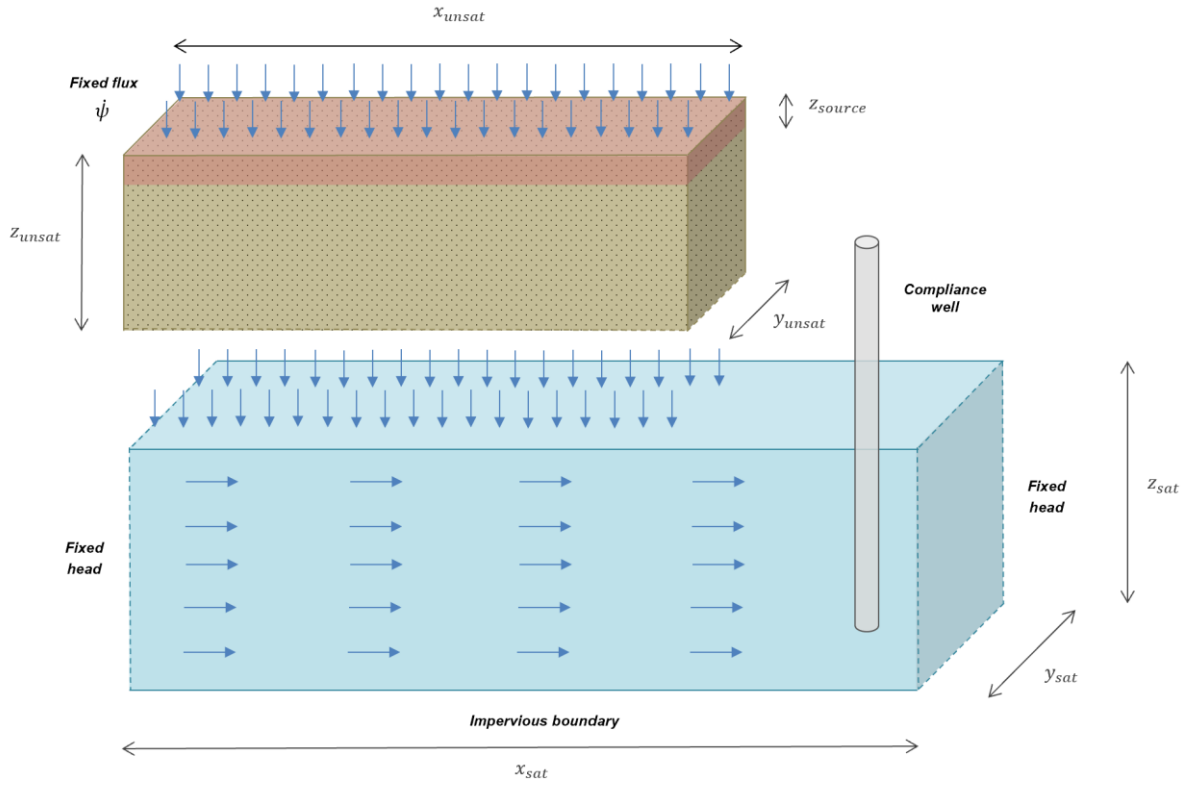


**Figure 5.** Conceptual model of the aquifer structure of $A_2$.

| Parameter | Symbol | Value | Unit | PDF | Source |
|---|---|---|---|---|---|
| Infiltration flux | $\dot{\psi}(t_0)$ | 3 | $mm\ day^{-1}\ m^{-2}$ | Exponential | (KIGAM, 1997; Lee and Song, 2007), (GIMS, 2025), Engineering judgement |
| Source depth | $z_{source}$ | 0.02 | $m$ | [−] | Engineering judgement |
| Unsaturated zone length | $x_{unsat}$ | 100 | $m$ | [−] | Engineering judgement |
| Unsaturated zone thickness | $y_{unsat}$ | 1 | $m$ | [−] | Engineering judgement |
| Unsaturated zone depth | $z_{unsat}$ | 2 | $m$ | [−] | Engineering judgement |
| Unsaturated zone longitudinal dispersivity | $\alpha_{L,unsat}$ | 0.2 | $m$ | [−] | Engineering judgement |
| Unsaturated zone saturation level | $S_{l,unsat}$ | 0.9 | [−] | [−] | Engineering judgement |
| Saturated zone length | $x_{sat}$ | 100 | $m$ | [−] | Engineering judgement |
| Saturated zone thickness | $y_{sat}$ | 1 | $m$ | [−] | Engineering judgement |
| Saturated zone depth | $z_{sat}$ | 5 | $m$ | [−] | Engineering judgement |
| Distribution coefficient of $^{137}$Cs (sand) | $K_{d,^{137}Cs}^{sand}$ | $530 \pm 6$ | $l\ kg^{-1}$ | Gaussian | (Gil-García, Rigol and Vidal, 2009) |
| Distribution coefficient of $^{90}$Sr (sand) | $K_{d,^{90}Sr}^{sand}$ | $22 \pm 6$ | $l\ kg^{-1}$ | Gaussian | (Gil-García, Rigol and Vidal, 2009) |
| Distribution coefficient of $^{137}$Cs (loam) | $K_{d,^{137}Cs}^{loam}$ | $3500 \pm 4$ | $l\ kg^{-1}$ | Gaussian | (Gil-García, Rigol and Vidal, 2009) |
| Distribution coefficient of $^{90}$Sr (loam) | $K_{d,^{90}Sr}^{loam}$ | $57 \pm 6$ | $l\ kg^{-1}$ | Gaussian | (Gil-García, Rigol and Vidal, 2009) |

| | | | | | |
|---|---|---|---|---|---|
| Saturated zone longitudinal dispersivity | $\alpha_{L,sat}$ | 10 | $m$ | $[-]$ | Engineering judgement |
| Saturated zone saturation level | $S_{l,sat}$ | 1 | $[-]$ | $[-]$ | Engineering judgement |
| Saturated zone hydraulic conductivity | $K_{sat}$ | $10^{-5}$ | $m\ s^{-1}$ | $[-]$ | (Lee and Song, 2007) |
| Hydraulic gradient | $\nabla h$ | 0.01 | $[-]$ | $[-]$ | (KIGAM, 1997) |
| $^{137}$Cs dose conversion factor (adult) | $DC_{^{137}Cs}$ | $1.3 \cdot 10^{-8}$ | $Sv\ Bq^{-1}$ | $[-]$ | (ICRP, 2012) |
| $^{90}$Sr dose conversion factor (adult) | $DC_{^{90}Sr}$ | $2.8 \cdot 10^{-8}$ | $Sv\ Bq^{-1}$ | $[-]$ | (ICRP, 2012) |
| Water consumption | $V_W$ | 730 | $l\ year^{-1}$ | $[-]$ | (Cadini, Tosoni and Zio, 2016) |

**Table 6.** List of parameters used for the GoldSim model of $A_2$.

### 3.5 Monte Carlo simulation

The following assumptions are undertaken to operationalize the Monte Carlo simulation (Figure 2):

- A set of $N_s = 10^6$ Monte Carlo trials are run for the evaluation of the dispersion model. To model the marginal PDFs of the deposited concentrations of $^{90}$Sr and $^{137}$Cs, a truncated Gamma PDF is chosen from a pool of candidate distributions through model selection testing by employing Akaike Information Criterion (AIC) (Mutua, 1994).
- A set of $N_g = 10^3$ Monte Carlo trials are run for the evaluation of the groundwater contaminant transport model and the estimation of the $D_{peak}$ distribution.
- An importance sampling algorithm (GoldSim, 2021b) is adopted to characterize the right tail of the deposited ST PDFs, to ensure its representativeness using a limited number $N_g$ of Monte Carlo trials and to limit the computational effort required by the analysis.
- An empirically estimated Pearson correlation coefficient $\rho(^{137}\text{Cs}, ^{90}\text{Sr})$ is imposed between the samples drawn from the fitted PDFs of $^{137}$Cs and $^{90}$Sr (Iman and Conover, 1982).
- The analysis of the scenarios listed in Table 1 are conducted with the same seeds of the random number generators adopted throughout the sampling of the parameters used to feed the atmospheric dispersion and the groundwater contaminant transport models, to guarantee that the scenarios outcomes are fairly compared.

## 4. Results and discussion

The effect of CC on the PSA outcomes are discussed in terms of Conditional Value at Risk (CVaR) (Dixit, Verma and Tiwari, 2020; Di Maio, Tonicello and Zio, 2022):

$$CVaR(D_{peak}) = \mathbb{E}[D_{peak}|D_{peak} > \tau] \tag{11}$$

and exceedance probability $P_{ex}$ (Chang and Shinozuka, 2004; Di Maio, Tonicello and Zio, 2022):

$$P_{ex} = \frac{N_{ex}}{N_g} \tag{12}$$

where $\tau$ is the regulatory threshold corresponding to the dose limit for drinking water, in this work conservatively assumed equal to $10^{-4}$ Sv/year (Park *et al.*, 2021), and $N_{ex}$ is the number of simulations in which $D_{peak} > \tau$.

### 4.1 Results for the aquifer located in $A_1$

The Complementary Cumulative Density Function (CCDF) of $D_{peak}$ for the aquifer located in $A_1$ is presented in Figure 6 for each CC impact scenario listed in Table 1. As it can be seen, the CCDFs shift to the right, i.e., to high dose levels, as the SB IE frequency variation $\alpha_{SB}$ due to CC increases with respect to the *Baseline* scenarios and $\beta$ increases. In other words, wetter CBCs lead to larger $D_{peak}$, whereas drier CBCs lead to lower $D_{peak}$. In the end, the worst scenario is due to the combination of SB frequency increase and wetter CBCs, i.e., *CC-induced*$_{Wet}$, whereas the scenario with the lowest $D_{peak}$ results from the combination of no SB frequency increase and drier CBC, i.e., *Baseline*$_{Dry}$. Nevertheless, $D_{peak}$ CCDFs span in a range from $10^{-9}$ to $10^{-4}$ Sv/yr, meaning that the probability of exceeding $\tau$ is extremely small.

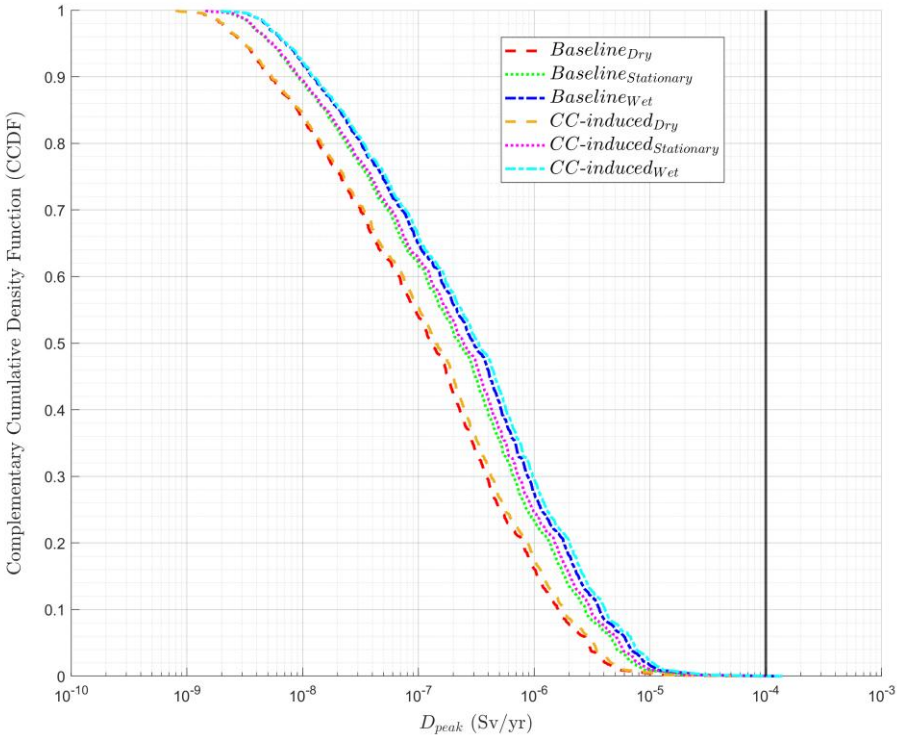


**Figure 6.** Peak dose CCDFs for the aquifer located in $A_1$.

The PDF of the breakthrough time $t_{peak}$ is presented for each scenario in Figure 7. In this case, only CBCs variations lead to a notable difference with respect to the *Baseline* case since the variation of $t_{peak}$ is only induced by the imposed CBC (i.e., the hydraulic boundary condition). Moreover, the effect of the CC-related assumptions is opposite to that for $D_{peak}$ (wetter scenarios lead to higher $D_{peak}$ whereas drier scenarios lead to lower $D_{peak}$ with respect to *Baseline*), namely, wetter CBCs lead to a lower $t_{peak}$ whereas drier CBCs lead to a higher $t_{peak}$, as physically expected (Govindaraju and Das, 2007).

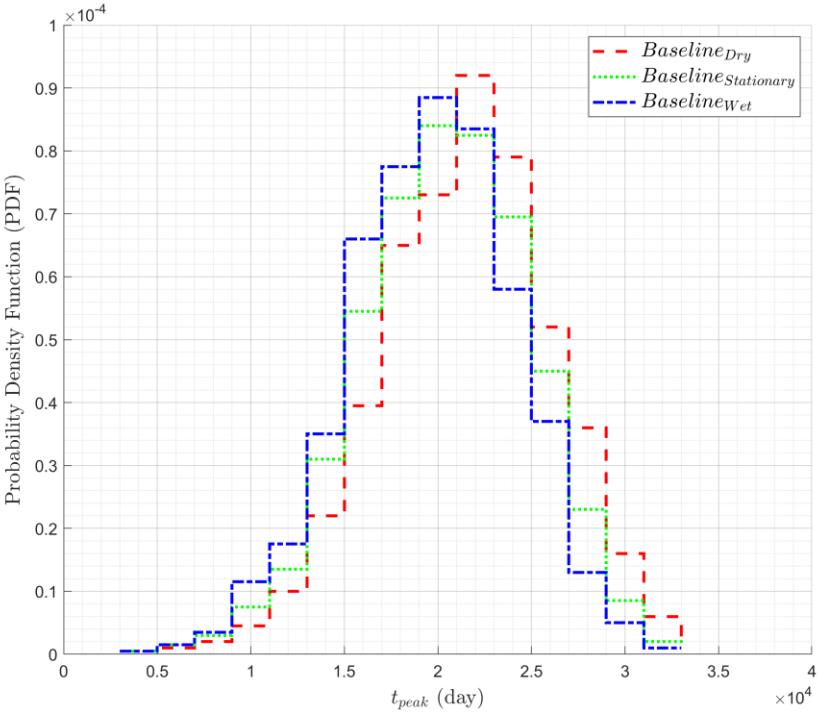


**Figure 7.** Breakthrough time PDFs for the aquifer located in $A_1$.

The CVaR and $P_{ex}$ of $D_{peak}$ are shown in Figure 8 to highlight the risk relevance of the results.

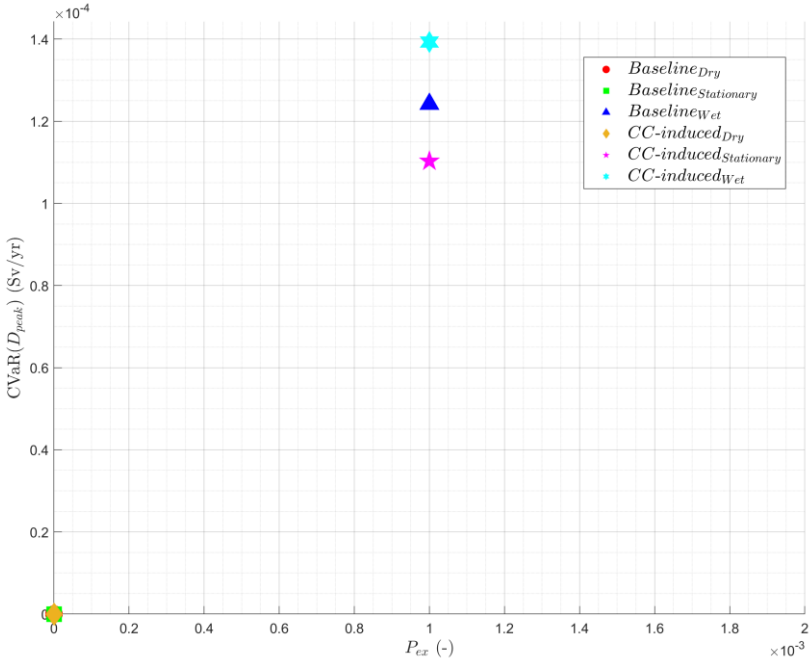


**Figure 8.** Scatter plot of CVaR ($y$-axis) versus $P_{ex}$ ($x$-axis) for the aquifer located in $A_1$. Both metrics are referring to values of $D_{peak}$ exceeding the regulatory threshold of $\tau = 10^{-4}$ Sv/yr (Park *et al.*, 2021).

It can be seen that only some CC-related scenarios lead to $P_{ex} > 0$, meaning that CC plays a relevant role for exceeding $\tau$ in the future. Also, CVaR shows that extreme wetter CBCs are more important than the increase of frequency of the SB IE (CVaR associated to $Baseline_{Wet}$ scenario (blue triangle) is higher than the one related to $CC\text{-}induced_{Stationary}$ scenario (magenta star)). In summary, CC effects need to be considered in the PSA to avoid underestimating the environmental consequences of a NPP severe accident in terms of groundwater contamination.

### 4.2 Results for the aquifer located in $A_2$

The $D_{peak}$ CCDFs for the aquifer located in $A_2$ are presented in Figure 9. Also in this case, the same considerations drawn from the results of $A_1$ hold true. Nevertheless, in this case, the CCDFs are shifted on higher average dose levels for all scenarios (including *Baseline*) and span in a range from $10^{-8}$ to $10^{-4}$ Sv/yr. Moreover, a clear overlapping between $\tau$ and the CCDFs right tails is observable.

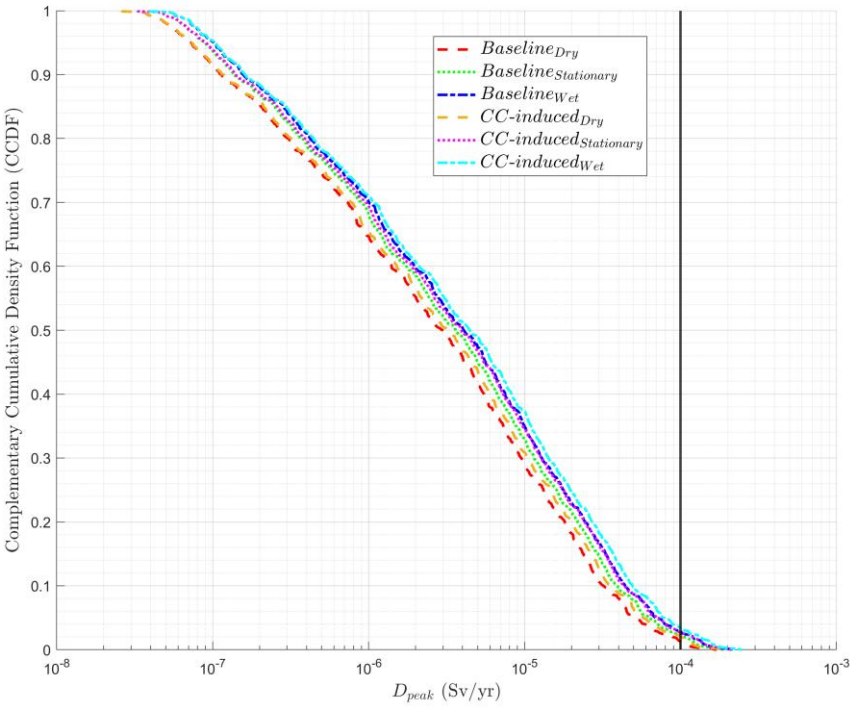


**Figure 9.** Peak dose CCDFs for the aquifer located in $A_2$.

The PDFs of $t_{peak}$ for the aquifer located in $A_2$ are presented in Figure 10. Also in this case, the same considerations regarding the role of wetter or drier CBCs hold true. Nevertheless, in this specific case a greater difference between the different $\beta$-related assumptions is evident, i.e., the PDFs of the different scenarios exhibit less overlap and more pronounced skewness with respect to the ones plotted in Figure 7, indicating that the aquifer located in $A_2$ is more sensitive to CBCs variations than the aquifer located in $A_1$ (possibly due to the unconfined structure of $A_2$). Specifically, the PDFs of the $t_{peak}$ for the $Baseline_{Dry}$ and $Baseline_{Wet}$ cases are more negatively skewed than the PDF of $t_{peak}$ for the $Baseline_{Stationary}$ case.

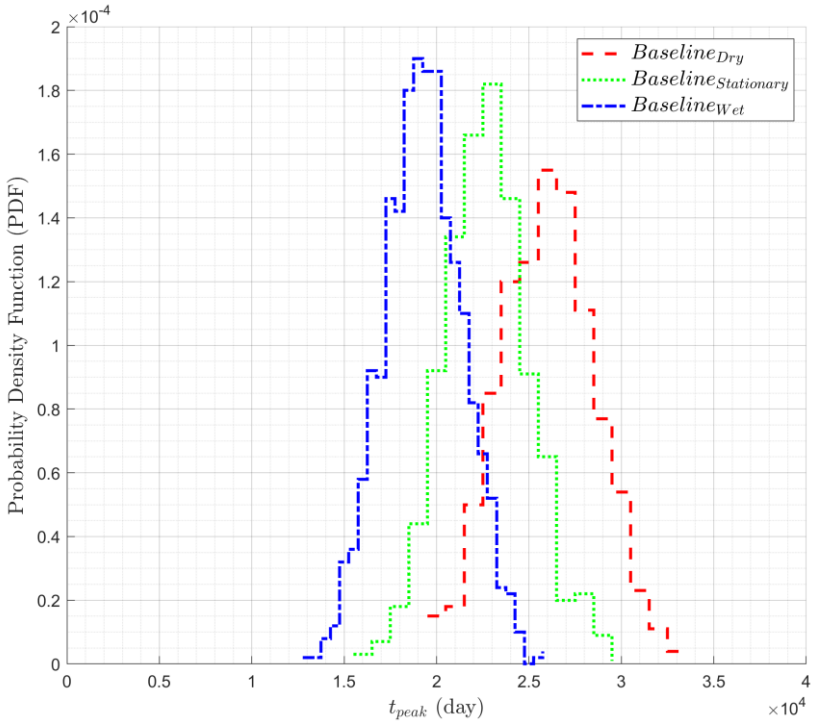


**Figure 10.** Breakthrough time PDFs for the aquifer located in $A_2$.

The CVaR and $P_{ex}$ for the aquifer located in $A_2$ are shown in Figure 11. In this case, for every CC impact scenario $P_{ex} > 0$, and it is an order of magnitude higher than the values previously calculated for the aquifer located in $A_1$. Moreover, in this case, it can be observed that the maximum spread of the risk metrics, i.e., the interval between the best and worst outcomes across all scenarios, is in the range $[0.013, 0.035]$ for $P_{ex}$ and $[1.23 \cdot 10^{-4}, 1.45 \cdot 10^{-4}]$ Sv/yr for CVaR. In addition, the comparison of Figure 11 and Figure 8 highlights that the introduction of CC effects can have an important impact on the calculation of risk metrics related to the $D_{peak}$ from contaminated groundwater ingestion, even if the magnitude of such effects is strictly controlled

by the aquifer hydrogeological structure i.e., unconfined aquifers are more susceptible to fallout contamination, resulting in higher peak doses under otherwise identical conditions. This highlights that the vulnerability and risks associated with CC are spatially heterogeneous and require a tailored methodology, i.e., case study-dependent, to be properly evaluated. For the sake of comparison, in Table 7, the numerical results of the CVaR and $P_{ex}$ for $A_1$ and $A_2$ are reported.

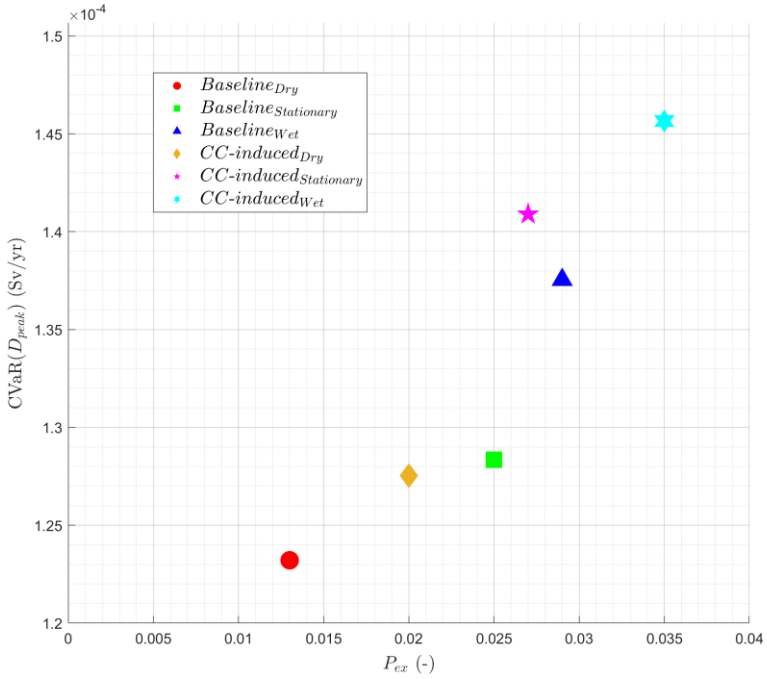


**Figure 11.** Scatter plot of CVaR ($y$-axis) versus $P_{ex}$ ($x$-axis) for the aquifer located in $A_2$. Both metrics are referring to values of $D_{peak}$ exceeding the regulatory threshold of $\tau = 10^{-4}$ Sv/yr (Park *et al.*, 2021).

| Scenario | $A_1$ | | $A_2$ | |
|---|---|---|---|---|
| $Baseline_{Dry}$ | $P_{ex} = 0$ | $CVaR = 0$ | $P_{ex} = 1.3\ 10^{-2}$ | $CVaR = 1.23\ 10^{-4}$ |
| $Baseline_{Stationary}$ | $P_{ex} = 0$ | $CVaR = 0$ | $P_{ex} = 2.8\ 10^{-2}$ | $CVaR = 1.28\ 10^{-4}$ |
| $Baseline_{Wet}$ | $P_{ex} = 10^{-3}$ | $CVaR = 1.22\ 10^{-4}$ | $P_{ex} = 2.9\ 10^{-2}$ | $CVaR = 1.37\ 10^{-4}$ |
| $CC\text{-}induced_{Dry}$ | $P_{ex} = 0$ | $CVaR = 0$ | $P_{ex} = 2.0\ 10^{-2}$ | $CVaR = 1.27\ 10^{-4}$ |
| $CC\text{-}induced_{Stationary}$ | $P_{ex} = 10^{-3}$ | $CVaR = 1.15\ 10^{-4}$ | $P_{ex} = 2.7\ 10^{-2}$ | $CVaR = 1.41\ 10^{-4}$ |
| $CC\text{-}induced_{Wet}$ | $P_{ex} = 10^{-3}$ | $CVaR = 1.39\ 10^{-4}$ | $P_{ex} = 3.5\ 10^{-2}$ | $CVaR = 1.46\ 10^{-4}$ |

**Table 7.** CVaR and $P_{ex}$ values calculated for $A_1$ and $A_2$.

4.3 Implications for risk-informed decision making

The results presented in Section 4.1 and Section 4.2 highlight the added value of performing a bounding analysis with the proposed simulation-based PSA framework; the evaluation of multiple CC scenarios enables the assessment of the possible high-level consequences of CC on PSA outputs even in the case of substantial uncertainty on the magnitude of such effects. Specifically, in Figure 12 the relative differences ΔCVaR and $\Delta P_{ex}$ between each CC scenario and the $Baseline_{Stationary}$ values of CVaR and $P_{ex}$ are reported for the aquifer located in $A_2$, which has resulted more exposed to fallout contamination. The results of the $Baseline_{Stationary}$ scenario are taken as the reference values representative of the PSA outcome when CC-related effects are not considered. As shown in Figure 12, ΔCVaR and $\Delta P_{ex}$ increase more in the upper right quadrant of the ΔCVaR$-\Delta P_{ex}$ plane with respect to the lower left quadrant of the ΔCVaR$-\Delta P_{ex}$ plane, showing the non-linear response between CC-related assumptions and PSA outcomes. In this specific case, the assumptions related to the realization of wetter future conditions, i.e., $Baseline_{Wet}$ and $CC\text{-}induced_{Wet}$, increase substantially the risk associated to aquifer contamination and this, underlines the relevance of considering CC-related effects in the risk assessment of the environmental consequences of NPP severe accidents.

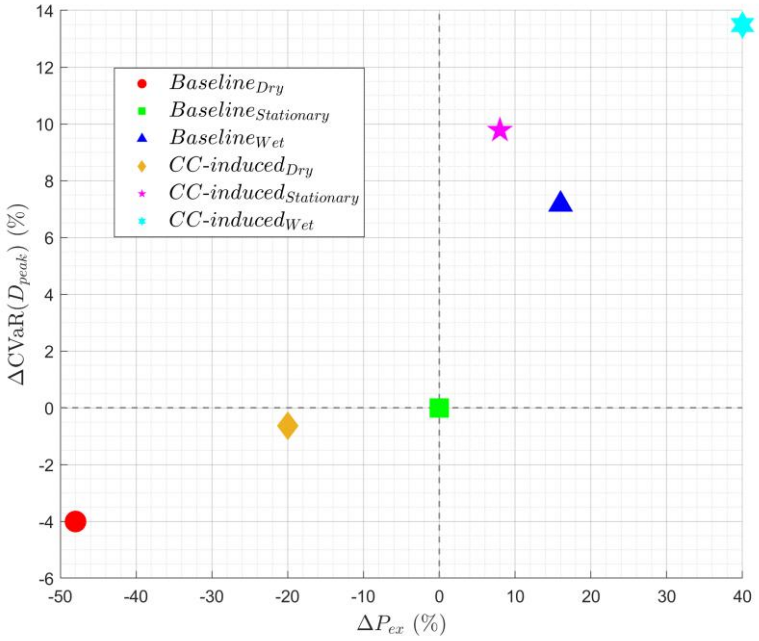


**Figure 12.** Scatter plot of ΔCVaR ($x$-axis) versus $\Delta P_{ex}$ ($y$-axis) for the aquifer located in $A_2$. For both metrics the reference scenario for the calculation of the relative differences is $Baseline_{Stationary}$.

Indeed, by assuming the perspective of a highly risk-averse decision maker, quantitative metrics like $P_{ex}$ and CVaR enable the calculation of the expected maximum loss in the case of the worst-case CC scenario. Instead, by assuming the perspective of a moderately risk-averse decision maker, these metrics could guide the risk-constrained optimization of possible NPP CC resilience strategies by comparing the maximum expected loss incurred when these strategies are not implemented.

## 5. Conclusions

In this paper, a computational framework for PSA of NPPs has been presented, capable of accounting for the CC-induced effects on long-term dose due to contaminated groundwater ingestion. The framework couples *i*) a CC impact assessment model, *ii*) a ST estimation model, *iii*) an atmospheric dispersion model, *iv*) a groundwater contaminant transport model, to quantify and propagate the uncertainties arising from CC related variables during the accident development, i.e., starting from the ST release (L1-L2 PSA), through the atmospheric dispersion and fallout deposition processes (L3 PSA), until the aquifer contamination (L3 PSA). The impacts of CC are introduced both at the L1 PSA interface, i.e., in terms of IEs frequency increase and at the L3 PSA interface, i.e., wetter or drier aquifer CBCs. The framework is exemplified on a case study related to a multi-unit NPP located in South Korea to evaluate the environmental impact of a hypothetical severe accident on two nearby aquifers. The results, provided in terms of CVaR and probability of exceedance of the regulatory dose limit, highlight that CC can be relevant for safety-related decision-making. Specifically, under the assumptions made in the considered case study, due to CC both the CVaR and the probability of exceedance of the regulatory dose limit are increased, so that, NPPs safety barriers should be designed considering also the CC contribution to dose exceedance.

**Acknowledgement**

The work of Thomas Matteo Coscia and Enrico Zio is supported by PE RETURN SPOKE VS4 (CUP D43C22003030002, codice progetto PE0000005), for the project titled “MULTI RISK SCIENCE FOR RESILIENT COMMUNITIES UNDER A CHANGING CLIMATE”, funded by the NextGenerationEU – Piano Nazionale di Ripresa e Resilienza (PNRR) (Missione 4, componente 2, Investimento 1.3).

**Appendix A**

The multiplicative factor $\alpha_i$ of Eq. 1 is defined as:

$$\alpha_i = \frac{f_i(T)}{f_i(t_0)} = \frac{\mathcal{F}_i(m(T))\,\mathcal{T}_r\big(m(T)\big)^{-1}}{\mathcal{F}_i(m(t_0))\,\mathcal{T}_r\big(m(t_0)\big)^{-1}} \tag{A.1}$$

where at a generic time $t$, the frequency of occurrence of the $i$-th IE $f_i$, $i = 1,2,\dots,I$, is equal to (IAEA, 1993; Kumar *et al.*, 2017):

$$f_i(t) = \mathcal{F}_i(m(t))\,\mathcal{T}_r\big(m(t)\big)^{-1} \tag{A.2}$$

where $\mathcal{F}_i\big(m(t)\big)$ is the fragility curve that maps the probability of the $i$-th IE occurring conditional to the hazard induced by a climatic variable $m(t)$ and $\mathcal{T}_r\big(m(t)\big)$ is the return time of the hazard intensity induced by $m(t)$, which typically is defined by regulation (it is worth mentioning that Eq. A.2 is applicable in the context of a bounding analysis of external IEs (U.S. Nuclear Regulatory Commission, 2020)).

If $m(\cdot)|\mathcal{T}_r$ are evaluated for the same return period, i.e., $\mathcal{T}_r\big(m(T)\big) = \mathcal{T}_r\big(m(t_0)\big) = \mathcal{T}_r$, Eq. A.1 simplifies to:

$$\alpha_i = \frac{\mathcal{F}_i(m(T)|\mathcal{T}_r)}{\mathcal{F}_i(m(t_0)|\mathcal{T}_r)} \tag{A.3}$$

Under the assumptions that the fragility curve $\mathcal{F}_i(\cdot)$ is time invariant and differentiable, the numerator of Eq. A.3 can be expanded in a Taylor series truncated to the first order:

$$\alpha_i \cong \frac{\mathcal{F}_i(m(t_0)|\mathcal{T}_r) + \mathcal{F}_i'(m(t_0)|\mathcal{T}_r)(m(T)|\mathcal{T}_r - m(t_0)|\mathcal{T}_r)}{\mathcal{F}_i(m(t_0)|\mathcal{T}_r)} \tag{A.4}$$

if $\varepsilon_i = \frac{\mathcal{F}_i'(m(t_0)|\mathcal{T}_r)}{\mathcal{F}_i(m(t_0)|\mathcal{T}_r)}$, Eq. A.4 reduces to Eq. A.5, that corresponds to Eq. 2 of Section 2.1:

$$\alpha_i \cong 1 + \varepsilon_i\,(m(T)|\mathcal{T}_r - m(t_0)|\mathcal{T}_r) \tag{A.5}$$

**Appendix B**

For the case study presented in Section 3, the $i$-th IE considered is the SB caused by flooding due to an extreme precipitation event. Therefore, $m(x, y, t)$ is the maximum annual daily cumulative precipitation level in the location $(x, y)$. For $\mathcal{T}_r = 50$ yr, $m(t_0)|\mathcal{T}_r = 220$ mm and $m(T)|\mathcal{T}_r = 315.2$ mm (Shin et al. 2021). To model the NPP SSCs fragility to flooding the log-normal fragility curve plotted in Figure B.1 has been employed (B. J. Kim, Kim, Hahm, and Han 2021): $m(t_0)|\mathcal{T}_r$ returns $\varepsilon_i = 0.095$.

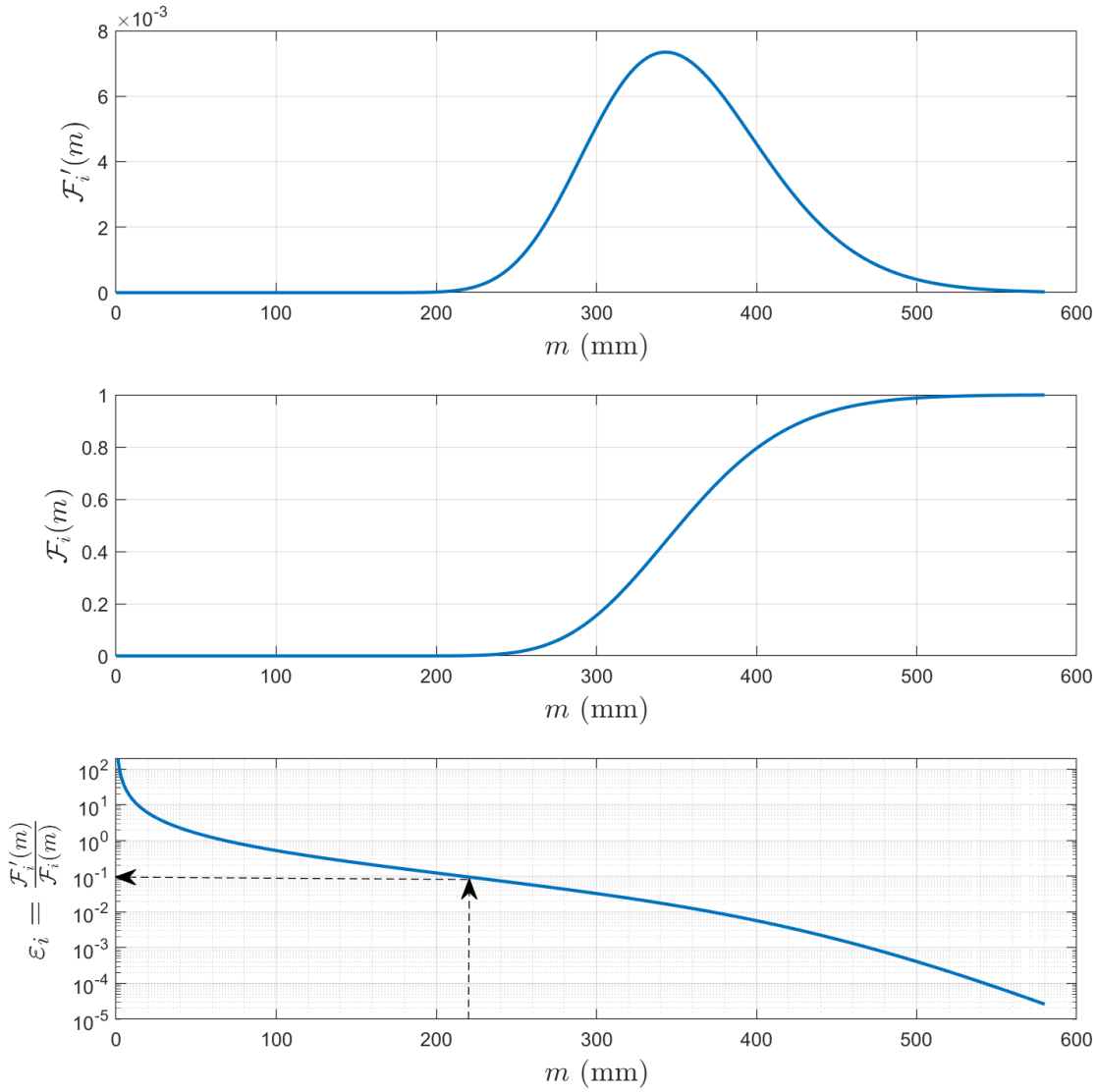


**Figure B.1.** Log-normal flooding fragility curve $\mathcal{F}_i(m)$, its derivative $\mathcal{F}_i'(m)$ and $\varepsilon_i(m)$.

## Appendix C

The PMF $P_n$ of Eq. 9 is motivated by the results provided in (Marchetti, Di Maio and Zio, 2025). Figure C.1 shows the fitting of the PMFs listed in Table C.1 to the probability that $n = 1, 2, 3, 4$ units of a multi-unit NPP fail due to the same IE. The lowest Akaike Information Criterion (AIC) is provided by the Truncated Poisson, then by the Truncated Negative Binomial, finally by the Truncated Discrete Exponential that is the only distribution that does not underestimate the probability of $n = 4$ units failure. Thus, in this work a Truncated Discrete Exponential is conservatively adopted in Eq. 9.

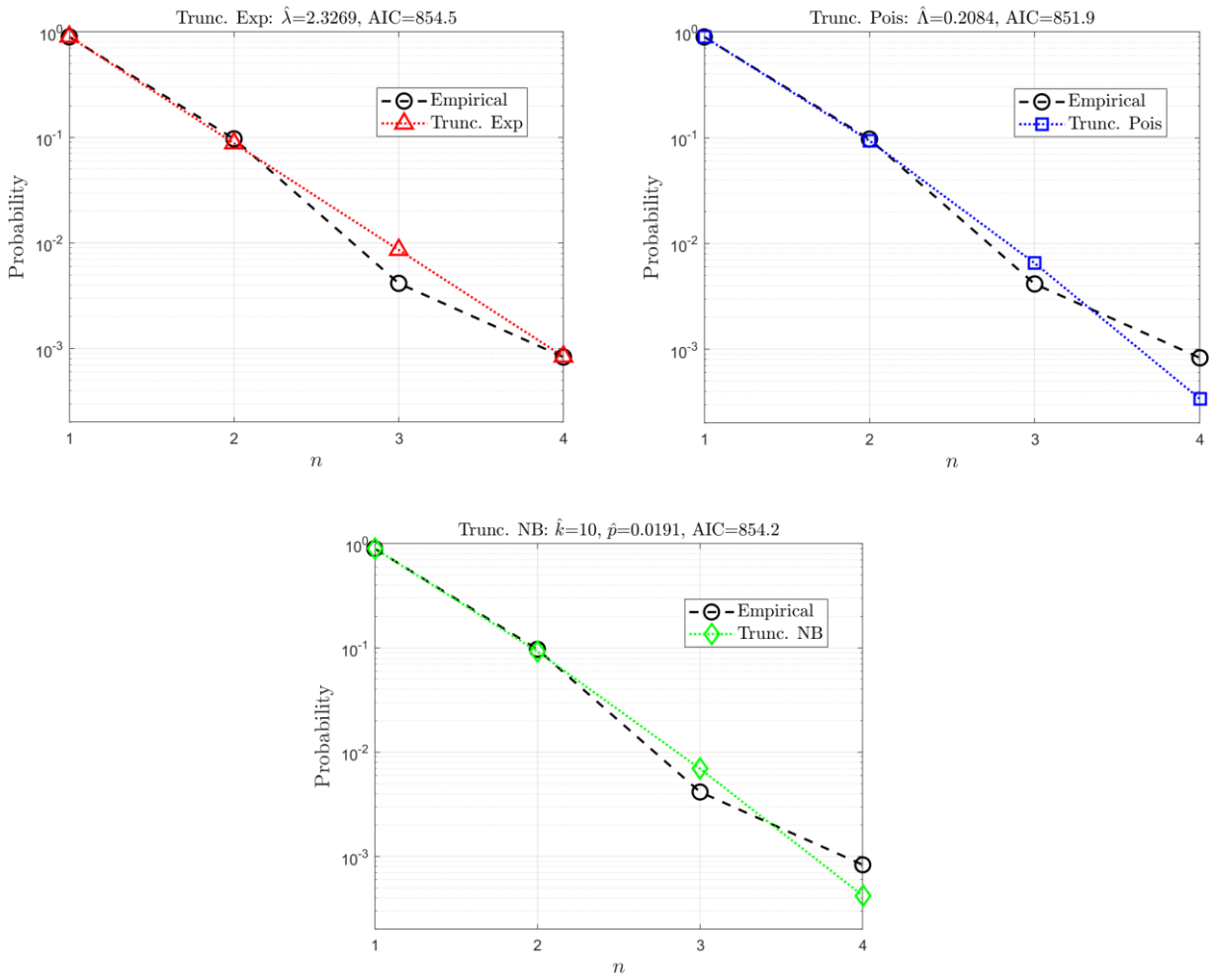


**Figure C.1.** Comparison between the fitted PMFs and the empirical PMF.

| Distribution | Shape | Parameters | Source |
|---|---|---|---|
| Truncated Discrete Exponential | $P_n = \frac{e^{\lambda} - 1}{1 - e^{-\lambda N}}\ e^{-\lambda n}$ | $\lambda > 0$ | (Berber, 2017) |
| Truncated Poisson | $P_n = \frac{\Lambda^n\ e^{-\Lambda}}{n!}(1 - e^{-\Lambda})$ | $\Lambda > 0$ | (Plackett, 1953) |
| Truncated Negative Binomial | $P_n = \frac{w^k\ (k+n-1)!}{1 - w^k\ (k-1)!\ n!}\ \eta^n$ <br> $\begin{cases} w = 1/(1+p) \\ \eta = (1-w) \end{cases}$ | $p \in [0,1]$ <br> $k \in \mathbb{N}$ | (Sampford, 1955; Brass, 1958) |

**Table C.1.** The employed truncated discrete distributions.

**References**


Ali, A.M. and Kakosimos, K.E. (2023) 'A receptor-centric decision support system for the mitigation of nuclear power atmospheric release incidents', *Reliability Engineering & System Safety*, 238, p. 109474. Available at: https://doi.org/10.1016/j.ress.2023.109474.

An, H.Y. *et al.* (2016) 'Atmospheric Dispersion Characteristics of Radioactive Materials according to the Local Weather and Emission Conditions', *Journal of Radiation Protection and Research*, 41(4), pp. 315–327. Available at: https://doi.org/10.14407/jrpr.2016.41.4.315.

Ashley, S.F. *et al.* (2017) 'Predicting the cost of the consequences of a large nuclear accident in the UK', *Process Safety and Environmental Protection*, 112, pp. 96–113. Available at: https://doi.org/10.1016/j.psep.2017.08.032.

Ayoub, A. and Sornette, D. (2023) 'The power of precursors: An empirical assessment of nuclear power risks', *Progress in Nuclear Energy*, 164. Available at: https://doi.org/10.1016/j.pnucene.2023.104878.

Baek, S. and Heo, G. (2023) 'Development of dynamic integrated consequence evaluation (DICE) for dynamic event tree approaches: Numerical validation for a loss of coolant accident', *Reliability Engineering & System Safety*, 238, p. 109425. Available at: https://doi.org/10.1016/j.ress.2023.109425.

Berber, S. (2017) 'The Exponential, Gaussian and Uniform Truncated Discrete Density Functions for Discrete Time Systems Analysis', *WSEAS TRANSACTIONS on MATHEMATICS*, 16, pp. 226–238.

Biwalkar, R. *et al.* (2023) 'Estimation of Near-Field and Far-Field Post-Accident Atmospheric Dispersion for Microreactors', *Nuclear Science and Engineering*, 197(8), pp. 2099–2116. Available at: https://doi.org/10.1080/00295639.2023.2204174.

Brass, W. (1958) 'Simplified Methods of Fitting the Truncated Negative Binomial Distribution', *Biometrika*, 45, pp. 59–68. Available at: https://about.jstor.org/terms.

Cadini, F., Tosoni, E. and Zio, E. (2016) 'Modeling the release and transport of 90Sr radionuclides from a superficial nuclear storage facility', *Stochastic Environmental Research and Risk Assessment*, 30(2), pp. 693–712. Available at: https://doi.org/10.1007/s00477-015-1112-7.

CCKP (2025) *Climate Change Knowledge Portal, for Development Practitioners and Policy Makers*. Available at: https://climateknowledgeportal.worldbank.org/country/korea-rep/climate-data-projections (Accessed: 27 January 2025).

la Cecilia, D. *et al.* (2020) 'Probabilistic indicators for soil and groundwater contamination risk assessment', *Ecological Indicators*, 115. Available at: https://doi.org/10.1016/j.ecolind.2020.106424.

Challa, V.S. *et al.* (2008) 'Sensitivity of atmospheric dispersion simulations by HYSPLIT to the meteorological predictions from a meso-scale model', *Environmental Fluid Mechanics*, 8(4), pp. 367–387. Available at: https://doi.org/10.1007/s10652-008-9098-z.

Chang, S.E. and Shinozuka, M. (2004) 'Measuring Improvements in the Disaster Resilience of Communities', *Earthquake Spectra*, 20(3), pp. 739–755. Available at: https://doi.org/10.1193/1.1775796.

Choun, Y.S. and Kim, M.K. (2019) 'Logic tree approach for probabilistic typhoon wind hazard assessment', *Nuclear Engineering and Technology*, 51(2), pp. 607–617. Available at: https://doi.org/10.1016/j.net.2018.11.006.

Coscia, T.M., Di Maio, F. and Zio, E. (2025) 'A modelling framework to analyze climate change effects on radionuclide aquifer contamination', *Journal of Contaminant Hydrology*, 269, p. 104470. Available at: https://doi.org/10.1016/j.jconhyd.2024.104470.

Denning, R. and Mubayi, V. (2017) 'Insights into the Societal Risk of Nuclear Power Plant Accidents', *Risk Analysis*, 37(1), pp. 160–172. Available at: https://doi.org/10.1111/risa.12590.

Dixit, V., Verma, P. and Tiwari, M.K. (2020) 'Assessment of pre and post-disaster supply chain resilience based on network structural parameters with CVaR as a risk measure', *International Journal of Production Economics*, 227, p. 107655. Available at: https://doi.org/10.1016/j.ijpe.2020.107655.

Draxler, R.R. and Hess, G.D. (1997) *Description of the HYSPLIT_4 modeling system. NOAA Technical Memorandum ERL ARL-224*.

Edwards, P.N. (2011) 'History of climate modeling', *Wiley Interdisciplinary Reviews: Climate Change*, 2(1), pp. 128–139. Available at: https://doi.org/10.1002/wcc.95.

Gil-García, C., Rigol, A. and Vidal, M. (2009) 'New best estimates for radionuclide solid–liquid distribution coefficients in soils, Part 1: radiostrontium and radiocaesium', *Journal of Environmental Radioactivity*, 100(9), pp. 690–696. Available at: https://doi.org/10.1016/J.JENVRAD.2008.10.003.

GIMS (2025) *National Groundwater Information Management and Service Center*. Available at: https://www.gims.go.kr/en/gims_start.do (Accessed: 12 March 2025).

GoldSim (2021a) ‘User’s Guide GoldSim Contaminant Transport Module, GoldSim Version 14.0 (October 2021), GoldSim Technology Group 255 S. King Street, Suite 800 Seattle, Washington 98104, USA’.
GoldSim (2021b) ‘User’s Guide GoldSim Probabilistic Simulation Environment, Version 14.0 (October 2021). GoldSim Technology Group 255 S. King Street, Suite 800 Seattle, Washington 98104, USA.’
Govindaraju, R.S. and Das, B.S. (2007) *Moment analysis for subsurface hydrologic applications*. Springer Science & Business Media.
IAEA (1993) *Defining initiating events for purposes of probabilistic safety assessment, IAEA-TECDOC-719*.
IAEA (2001) *Applications of probabilistic safety assessment (PSA) for nuclear power plants*.
IAEA (2024) *Development and Application of Level 1 Probabilistic Safety Assessment for Nuclear Power Plants*. Available at: www.iaea.org.
ICRP (2012) *Compendium of Dose Coefficients based on ICRP Publication 60. ICRP Publication 119. Ann. ICRP 41(Suppl.).*
Ilkka, K. (2018) *Seasonal and contextual factors in level 3 PSA Seasonal and contextual factors in level 3 PSA Probabilistic risk assessment method development and applications 114491/PRAMEA*.
Iman, R.L. and Conover, W.J. (1982) ‘A distribution-free approach to inducing rank correlation among input variables’, *Communications in Statistics - Simulation and Computation*, 11(3), pp. 311–334. Available at: https://doi.org/10.1080/03610918208812265.
KIGAM (1997) *Regional Assesment of Groundwater Resources (Hydrogeological Map of Younggwang Area, Korea vol.8), KR-97(C) -47*.
Kim, B.H., Song, M.J. and Cho, Y.S. (2022) ‘Safety Analysis of a Nuclear Power Plant against Unexpected Tsunamis’, *Sustainability (Switzerland)*, 14(20). Available at: https://doi.org/10.3390/su142013540.
Kim, B.J., Kim, M., Hahm, D., Park, J., *et al.* (2021) ‘Probabilistic flood assessment methodology for nuclear power plants considering extreme rainfall’, *Energies*, 14(9). Available at: https://doi.org/10.3390/en14092600.
Kim, B.J., Kim, M., Hahm, D. and Han, K.Y. (2021a) ‘Probabilistic flood hazard assessment method considering local intense precipitation at NPP sites’, *Journal of Hydrology*, 597. Available at: https://doi.org/10.1016/j.jhydrol.2021.126192.
Kim, B.J., Kim, M., Hahm, D. and Han, K.Y. (2021b) ‘Probabilistic flood hazard assessment method considering local intense precipitation at NPP sites’, *Journal of Hydrology*, 597. Available at: https://doi.org/10.1016/j.jhydrol.2021.126192.
Kim, G. *et al.* (2024a) ‘Probabilistic typhoon hazard and sensitivity analysis for nuclear power plant sites in Korea using logic tree’, *Progress in Nuclear Energy*, 176. Available at: https://doi.org/10.1016/j.pnucene.2024.105347.
Kim, G. *et al.* (2024b) ‘Probabilistic typhoon hazard and sensitivity analysis for nuclear power plant sites in Korea using logic tree’, *Progress in Nuclear Energy*, 176. Available at: https://doi.org/10.1016/j.pnucene.2024.105347.
Kim, G. *et al.* (2025) ‘Probabilistic safety assessment of off-site power system under typhoon considering failure correlation between transmission towers’, *Reliability Engineering & System Safety*, 254, p. 110637. Available at: https://doi.org/10.1016/j.ress.2024.110637.
Kim, G. and Heo, G. (2023) ‘Agent-based radiological emergency evacuation simulation modeling considering mitigation infrastructures’, *Reliability Engineering and System Safety*, 233. Available at: https://doi.org/10.1016/j.ress.2023.109098.
Kim, M.C. (2022) ‘Systematic approach and mathematical development for conditional core damage probabilities under station blackout of a nuclear power plant’, *Reliability Engineering & System Safety*, 217, p. 107969. Available at: https://doi.org/10.1016/j.ress.2021.107969.
Kim, M.K. and Choi, I.K. (2012) ‘A tsunami PSA methodology and application for NPP site in Korea’, *Nuclear Engineering and Design*, 244, pp. 92–99. Available at: https://doi.org/10.1016/j.nucengdes.2011.12.001.
Kim, R.H. *et al.* (2006) ‘Salinization properties of a shallow groundwater in a coastal reclaimed area, Yeonggwang, Korea’, *Environmental Geology*, 49(8), pp. 1180–1194. Available at: https://doi.org/10.1007/s00254-005-0163-3.
Kim, R.H. *et al.* (2019) ‘Hydrogeochemical characteristics of groundwater influenced by reclamation, seawater intrusion, and land use in the coastal area of Yeonggwang, Korea’, *Geosciences Journal*, 23(4), pp. 603–619. Available at: https://doi.org/10.1007/s12303-018-0065-5.

Kim, Y., Jang, S.C. and Lim, T.J. (2015) 'Hazard analysis of typhoon-related external events using extreme value theory', *Nuclear Engineering and Technology*, 47(1), pp. 59–65. Available at: https://doi.org/10.1016/j.net.2014.08.001.
Kim, Y.H. *et al.* (2020) 'Evaluation of the CMIP6 multi-model ensemble for climate extreme indices', *Weather and Climate Extremes*, 29. Available at: https://doi.org/10.1016/j.wace.2020.100269.
Kinser, A.M. (2001) *Simulating Wet Deposition of Radiocesium from the Chernobyl Accident. Theses and Dissertations. 4645*.
Kitamura, A. *et al.* (2015) 'Mathematical Modeling of Radioactive Contaminants in the Fukushima Environment', *Nuclear Science and Engineering*, 179(1), pp. 104–118. Available at: https://doi.org/10.13182/NSE13-89.
KMA (2025) *Korea Meteorological Administration, Open MET Data Portal*. Available at: https://data.kma.go.kr/resources/html/en/aowdp.html (Accessed: 10 March 2025).
Kumar, M. *et al.* (2017) 'Implementation of external hazards in level 1 and level 2 PSA: Considerations from the ASAMPSA_E project', in *Safety and Reliability - Theory and Applications - Proceedings of the 27th European Safety and Reliability Conference, ESREL 2017*. CRC Press/Balkema, pp. 3355–3363. Available at: https://doi.org/10.1201/9781315210469-423.
Lee, J.-Y. and Song, S.-H. (2007) 'Groundwater chemistry and ionic ratios in a western coastal aquifer of Buan, Korea: implication for seawater intrusion', *Geosciences Journal*, 11, pp. 259–270.
Lee, M. and Ko, Y.C. (2008) 'Quantification of severe accident source terms of a Westinghouse 3-loop plant', *Nuclear Engineering and Design*, 238(4), pp. 1080–1092. Available at: https://doi.org/10.1016/j.nucengdes.2007.09.003.
Lee, Y.M. and Choi, H.J. (2016) 'An evaluation of nuclide release from a trench-type LILW repository', *Progress in Nuclear Energy*, 88, pp. 95–103. Available at: https://doi.org/10.1016/j.pnucene.2015.11.014.
Libera, A. *et al.* (2019) 'Climate change impact on residual contaminants under sustainable remediation', *Journal of Contaminant Hydrology*, 226, p. 103518. Available at: https://doi.org/10.1016/J.JCONHYD.2019.103518.
Lim, H.-G., Han, S.H. and Yang, J.E. (2016) 'RESEARCH STATUS OF MULTI-UNIT PSA METHODOLOGY IN KOREA', in *13th International Conference on Probabilistic Safety Assessment and Management (PSAM 13)*. Available at: www.psam13.org.
Lim, J. *et al.* (2024) 'Methodology for estimating the contribution of forest fires in loss of offsite power events', *Nuclear Engineering and Technology* [Preprint]. Available at: https://doi.org/10.1016/j.net.2024.07.018.
Lotrecchiano, N. *et al.* (2020) 'Pollution dispersion from a fire using a Gaussian plume model', *International Journal of Safety and Security Engineering*, 10(4), pp. 431–439. Available at: https://doi.org/10.18280/ijsse.100401.
Di Maio, F., Tonicello, P. and Zio, E. (2022) 'A Modeling and Analysis Framework for Integrated Energy Systems Exposed to Climate Change-Induced NaTech Accidental Scenarios', *Sustainability 2022, Vol. 14, Page 786*, 14(2), p. 786. Available at: https://doi.org/10.3390/SU14020786.
Marchetti, S., Di Maio, F. and Zio, E. (2025) 'An Integrated Deterministic and Probabilistic Safety Assessment of Multi Unit Small Modular Reactors considering the degradation of shared safety barriers ', *Submitted to Nuclear Science and Engineering* [Preprint].
McGuffie, K. and Henderson-Sellers, A. (2001) 'Forty years of numerical climate modelling', *International Journal of Climatology*, 21(9), pp. 1067–1109. Available at: https://doi.org/10.1002/joc.632.
Meray, A. *et al.* (2024) 'Physics-informed surrogate modeling for supporting climate resilience at groundwater contamination sites', *Computers & Geosciences*, 183, p. 105508. Available at: https://doi.org/10.1016/j.cageo.2023.105508.
Mosleh, A. (2014) 'PRA: A Perspective on strengths, current Limitations, and possible improvements', *Nuclear Engineering and Technology*, 46(1), pp. 1–10. Available at: https://doi.org/10.5516/NET.03.2014.700.
Mutua, F.M. (1994) 'The use of the Akaike Information Criterion in the identification of an optimum flood frequency model', *Hydrological Sciences Journal*, 39(3), pp. 235–244. Available at: https://doi.org/10.1080/02626669409492740.
NOAA (2024) *https://www.ready.noaa.gov/archives.php*.
OECD (2021) *Climate Change: Assessment of the Vulnerability of Nuclear Power Plants and Approaches for their Adaptation, Nuclear Technology Development and Economics*.

Oh, K. *et al.* (2020) 'Study on multi-unit level 3 PSA to understand a characteristics of risk in a multi-unit context', *Nuclear Engineering and Technology*, 52(5), pp. 975–983. Available at: https://doi.org/10.1016/j.net.2019.11.005.
O'Neill, B.C. *et al.* (2016) 'The Scenario Model Intercomparison Project (ScenarioMIP) for CMIP6', *Geoscientific Model Development*, 9(9), pp. 3461–3482. Available at: https://doi.org/10.5194/gmd-9-3461-2016.
Park, J. *et al.* (2025) 'GPU-accelerated approaches for multi-unit level 3 PSA: Focusing on dispersion, evacuation, and dose assessment', *Reliability Engineering & System Safety*, 263, p. 111268. Available at: https://doi.org/10.1016/j.ress.2025.111268.
Park, S.J. *et al.* (2021) 'Safety assessment of second-phase disposal facility in Gyeongju low- and intermediate-level radioactive waste (LILW) repository using RESRAD-OFFSITE code', *Journal of Nuclear Science and Technology*, 58(11), pp. 1256–1265. Available at: https://doi.org/10.1080/00223131.2021.1936255.
Plackett, R.L. (1953) 'The Truncated Poisson Distribution', *Biometrics*, 9(4), pp. 485–488. Available at: https://www.jstor.org/stable/3001439.
Rolph, G., Stein, A. and Stunder, B. (2017) 'Real-time Environmental Applications and Display sYstem: READY', *Environmental Modelling and Software*, 95, pp. 210–228. Available at: https://doi.org/10.1016/j.envsoft.2017.06.025.
Roma, G., Di Maio, F. and Zio, E. (2024) 'A condition-informed dynamic Bayesian network framework to support severe accident management in nuclear power plants', *Reliability Engineering & System Safety*, 252, p. 110437. Available at: https://doi.org/10.1016/j.ress.2024.110437.
Sampford, M.R. (1955) 'The Truncated Negative Binomial Distribution', *Biometrika*, 42(1), pp. 58–69. Available at: https://about.jstor.org/terms.
Selivanova, A. *et al.* (2025) 'Creation of a System Dynamics model of recovery of affected areas after radioactive contamination', *Reliability Engineering & System Safety*, 260, p. 111031. Available at: https://doi.org/10.1016/j.ress.2025.111031.
Seneviratne, S.I. *et al.* (2012) 'Changes in Climate Extremes and their Impacts on the Natural Physical Environment', in *Managing the Risks of Extreme Events and Disasters to Advance Climate Change Adaptation*. Cambridge University Press, pp. 109–230. Available at: https://doi.org/10.1017/CBO9781139177245.006.
Shin, Yonggwan *et al.* (2021) 'Future Projections and Uncertainty Assessment of Precipitation Extremes in the Korean Peninsula from the CMIP6 Ensemble with a Statistical Framework'. Available at: https://doi.org/10.3390/atmos.
Sinha, V., Atikler, M. and Mileski, M. (2024) 'Atmospheric dispersion of radioactive materials for radiological risk assessment in case of hypothetical sodium cooled fast reactor accident', *Nuclear Engineering and Design*, 422. Available at: https://doi.org/10.1016/j.nucengdes.2024.113124.
Song, Y.H. *et al.* (2021) 'Advances in CMIP6 INM-CM5 over CMIP5 INM-CM4 for precipitation simulation in South Korea', *Atmospheric Research*, 247. Available at: https://doi.org/10.1016/j.atmosres.2020.105261.
Song, Y.H., Chung, E.S. and Shahid, S. (2022) 'Uncertainties in evapotranspiration projections associated with estimation methods and CMIP6 GCMs for South Korea', *Science of the Total Environment*, 825. Available at: https://doi.org/10.1016/j.scitotenv.2022.153953.
Tebaldi, C. *et al.* (2021) 'Climate model projections from the Scenario Model Intercomparison Project (ScenarioMIP) of CMIP6', *Earth System Dynamics*, 12(1), pp. 253–293. Available at: https://doi.org/10.5194/esd-12-253-2021.
Tolo, S., Patelli, E. and Beer, M. (2017) 'Robust vulnerability analysis of nuclear facilities subject to external hazards', *Stochastic Environmental Research and Risk Assessment*, 31(10), pp. 2733–2756. Available at: https://doi.org/10.1007/s00477-016-1360-1.
U.S. Nuclear Regulatory Commission (1996) *Initiating Event Rates at U.S. Nuclear Power Plants: 1987-1995 (NUREG/CR-5750)*. Available at: https://www.nrc.gov/docs/ML0618/ML061860698.pdf (Accessed: 12 March 2025).
U.S. Nuclear Regulatory Commission (2005) *Reevaluation of Station Blackout Risk at Nuclear Power Plants Analysis of Station Blackout Risk (NUREG/CR-6890, Vol. 2)*. Available at: https://www.nrc.gov/docs/ML0602/ML060200479.pdf (Accessed: 12 March 2025).
U.S. Nuclear Regulatory Commission (2016) *US Commercial Spent Nuclear Fuel Assembly Characteristics: 1968-2013 (NUREG/CR-7227)*. Available at: https://doi.org/https://doi.org/10.2172/1330516.

U.S. Nuclear Regulatory Commission (2020) *Regulatory Guide 1.200, Revision 3: Acceptability of Probabilistic Risk Assessment Results for Risk-Informed Activities*. Available at: https://www.nrc.gov/docs/ML2023/ML20238B871.pdf (Accessed: 21 May 2025).
Utsumi, N. and Kim, H. (2022) 'Observed influence of anthropogenic climate change on tropical cyclone heavy rainfall', *Nature Climate Change*, 12(5), pp. 436–440. Available at: https://doi.org/10.1038/s41558-022-01344-2.
Vododokhov, N., Erlandson, K. and Novog, D.R. (2025) 'CANDU Station Blackout D-PSA with RAVEN and TRACE Software', *Nuclear Science and Engineering*, pp. 1–20. Available at: https://doi.org/10.1080/00295639.2025.2455353.
Yan, R., Dunnett, S. and Andrews, J. (2023) 'A Petri net model-based resilience analysis of nuclear power plants under the threat of natural hazards', *Reliability Engineering & System Safety*, 230, p. 108979. Available at: https://doi.org/10.1016/j.ress.2022.108979.
Yang, J.E. (2018) 'Multi-unit risk assessment of nuclear power plants: Current status and issues', *Nuclear Engineering and Technology*, 50(8), pp. 1199–1209. Available at: https://doi.org/10.1016/j.net.2018.09.010.
Yavuz, C. (2023) 'Multi-Hazard Risk Assessment of South Korean Nuclear Power Plants', *Journal of Earthquake and Tsunami*, 17(3). Available at: https://doi.org/10.1142/S179343112350015X.
Yoon, J.Y., Kim, D.-S. and Han, S.H. (2024) 'A practical approach to treating time dependencies between diesel generator failures and offsite power recovery in multi-unit PSA', *Reliability Engineering & System Safety*, 245, p. 110013. Available at: https://doi.org/10.1016/j.ress.2024.110013.